The Pennsylvania State University

The Graduate School

Department of Materials Science and Engineering

OPTICAL AND VIBRATIONAL PROPERTIES OF TRANSITION METAL DICHALCOGENIDES HOMO- AND HETEROSTRUCTURES WITH TWISTED ORIENTATIONS

A Dissertation in

Materials Science and Engineering

by

Chanjing Zhou

Submitted in Partial Fulfillment
of the Requirements
for the Degree of

Doctor of Philosophy

August 2017

The dissertation of Chanjing Zhou was reviewed and approved* by the following:

Mauricio Terrones
Professor of Physics, Chemistry and Materials Science and Engineering
Dissertation Advisor
Chair of Committee

Suzanne Mohney
Professor of Materials Science and Engineering
Graduate Program Head of Materials Science and Engineering

Joshua Robinson
Professor of Materials Science and Engineering

Zhiwen Liu
Professor of Electrical Engineering

*Signatures are on file in the Graduate School

ABSTRACT

Van der Waals heterostructures have recently become a popular topic in the area of two-dimensional layered materials and beyond. This class of materials consists of stacked and coupled monolayers of the same or different materials via non-covalent bonding interactions. Examples of these materials include graphene, hexagonal-boron nitride and transition metal dichalcogenides (MX_2). Transition metal dichalcogenide (TMDCs) heterostructures are also potential candidates in the fabrication of novel optoelectronic devices, because of the direct bandgap and strong light-matter interactions in the visible spectra range of single-layered MX_2 (i.e. MoS_2 and WS_2) . There have been theoretical and experimental works describing that stacked MX_2 heterostructures can tune the electronic band structure of MX_2 with ultra-fast charge transfer properties that facilitate electron-hole separation.

In my thesis work, the chemical wet transfer method was used to fabricate stacked TMD bilayers. This involved several steps: The transfer process was optimized for better quality of the 2D crystals after transfer; the influence of the transfer process on the 2D materials was studied; and location-deterministic transfer was achieved by using a micro-manipulator under an optical microscope.

By the wet chemical transfer method, we successfully prepared stacked TMD bilayers including stacked MoS_2 homostructures and WS_2/MoS_2 heterostructures. These bilayers possessed various twisted angles, and Moiré patterns were formed due to the interference of the rotated lattices. The Moiré pattern can be regarded as a ‘super’ lattice, and its size is related to the twisted angle, bringing new properties other than the intrinsic nature of the TMD materials. We studied how the orientation of the twisted bilayers affect the properties of the homostructures and the heterostructures.

For stacked MoS_2 bilayer homostructures, it is found that the intensities of the Raman mode peaks are related to the twisted angles, while the photoluminescence intensities will reduce

after the coupling of the bilayer. In twisted WS_2/MoS_2 heterostructures, the symmetry is broken and the inter-layer coupling is affected due to the change of the van der Waals interaction between layers and also the change of chemical environment. From photoluminescence and low-frequency Raman of the heterostructures, we find that the charge transfer contributes more in heterostructures with small twisted angles due to better inter-layer coupling. The method of tuning charge transfer properties in TMDC heterostructures can open new possibilities in controlling the carrier densities in the individual layers, and therefore improving the performance of TMDC heterostructures in novel optoelectronic devices.

TABLE OF CONTENTS

LIST OF FIGURES

LIST OF TABLES

ACKNOWLEDGEMENTS

First of all, I would like to thank my family, who always support my decision and guide my life.

I would also like to thank my Ph.D. advisor, Dr. Mauricio Terrones, for giving me the opportunity to take part in the exciting project, for guiding me during the years of my graduate education, and for his valuable feedback on the research.

I thank the other members in my committee, Dr. Zhiwen Liu, Dr. Suzanne Mohney, and Dr. Joshua Robinson, for their expertise suggestions on the project.

At the same time, I would like to thank the financial support from the Chinese Fellowship Council and all the great help from them.

The last but not the least, I appreciate the help from my friends, their support and encouragement give me the courage to overcome all the problems.

Chapter 1

Introduction to the Transition Metal Dichalcogenide Heterostructures

1.1 Two dimensional materials beyond graphene

Two-Dimensional materials are crystalline atom-thick monolayers. For a long period of time, 2D materials were thought to be unstable at finite temperatures as predicted by thermodynamics [1]. However, when Geim, Novoselov and co-workers at Manchester University isolated graphene, a single-layer of sp^2 hybridized carbon in 2004 [2], it was shown that this is not the case. Since then, graphene and other quasi-2D materials including hexagonal boron nitride (h - BN) and transition metal dichalcogenides (TMDCs) have gained significant research interest due to their exceptional properties and potential for fabricating next generation electronic devices such as photovoltaic cells and semiconductors[3].

1.1.1 Graphene

Graphene, a two-dimensional sheet of sp^2-hybridized carbon atoms arranged in a hexagonal honeycomb lattice, is the basic building block of other carbon nanomaterials[4]. Graphene can be wrapped up to form fullerenes(0D), rolled to form carbon nanotubes(1D), or stacked to form graphite(3D)[5]. Free electrons from sp^2-hybridized carbon atoms form long-range π-conjugation in graphene. which yields extraordinary electrical, thermal and mechanical properties[3]. Graphene is a semi-conductor with zero band-gap between the conduction and valence bands. It also has an extremely high carrier mobility at room temperature which is about 2 orders of magnitudes greater than that of silicon[5]. Graphene is promising for potential use in

field effect transistors (FETs) due to the high mobility, high ON/OFF ratio of doped graphene, high compatibility with current devices and one atomic layer thickness[4].

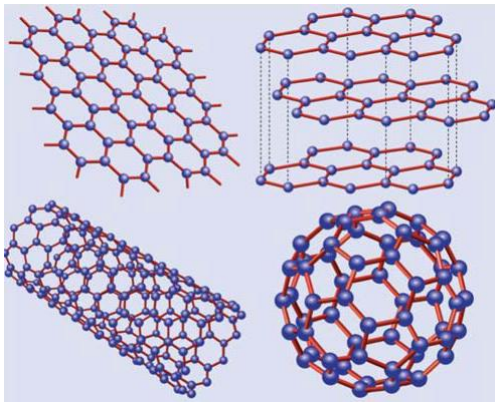

Figure 1-1. Structures of graphene (top left), 3D Graphite (top right), 1D Carbon nanotubes (bottom left), and 0D Fullerenes C_{60} (bottom right) [6].

1.1.2 Hexagonal boron nitride

Hexagonal boron nitride (h-BN) is a wide band gap (5.5 eV) III-V compound[7]. h-BN and a similarly structured carbon lattice are isoelectronic. BN exists in various crystalline forms: the hexagonal form (h-BN) analogue to graphite, the cubic form (c-BN) similar to diamond, and the rare wurtzite BN form (w-BN). Hexagonal BN consists of sp^2-bonded two-dimensional layers with alternating boron and nitrogen atoms in a honeycomb arrangement[8].The boron and nitrogen atoms are bound by strong σ bonds, and the reduced electron-delocalization results in a large band gap and little absorbance of visible light, making the h-BN colorless.

h-BN is an excellent insulator and a promising dielectric material due to the large band gap. Recently, BN-graphene hetero nanostructures have also drawn much attention. This is because BN can serve as a dielectric substrate for graphene resulting in carrier mobility as high as

~60000 cm^2 V^{-1} s^{-1}, which is 10 times higher than ones on SiO_2/Si substrates[9]. Besides, h-BN substrate can also provide graphene sheets with lower inhomogeneity[9].

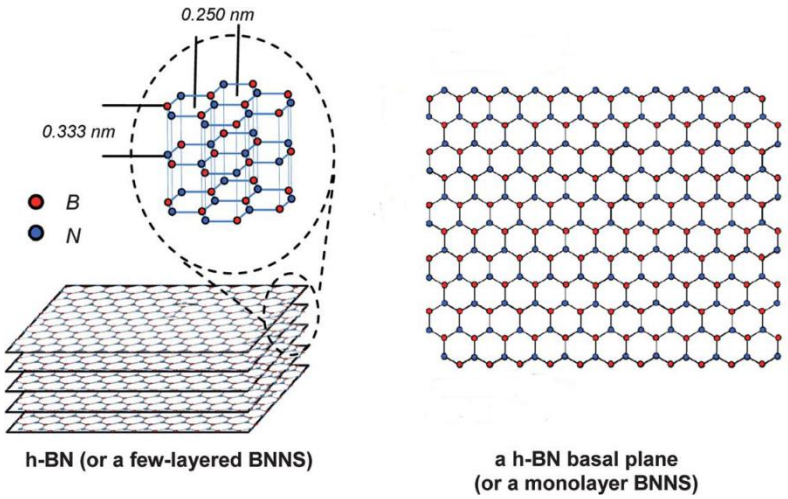

Figure 1-2. h-BN 2D structures. The red circles stand for boron atoms and blue circles stand for nitrogen atoms. The planar h-BN has a honeycomb structure and the insert image shows the AB stacking order [9].

1.1.3 Transition metal dichalcogenides (TMDCs)

Transition Metal Dichalcogenides (MX_2) consist of a "sandwich" structure with a hexagonal transition metal layer (M = Mo, W, Nb) between two hexagonal chalcogen layers (X = S, Se, Te)[10]. Depending on the stacking, MX_2 can form different crystal structures. Taking MoS_2 as an example, the Mo atoms can be coordinated in a trigonal prismatic center through ionic-covalent interactions with the six surrounding S atoms (1H phase) or in an octahedral center (1T phase) of six S atoms (see Figure 1-3).

Compared to graphene, TMDs possess sizable bandgaps around 1–2 eV [11] and the band gap is layer dependent. In the bulk, there is an indirect band gap and this turns into a direct band gap as the number of layers reduces to one. TMDs have gained an explosion of attention in recent

years due to these exciting properties and are being heavily researched for use in FETs, photodetectors, DNA detection, and memory devices[10].

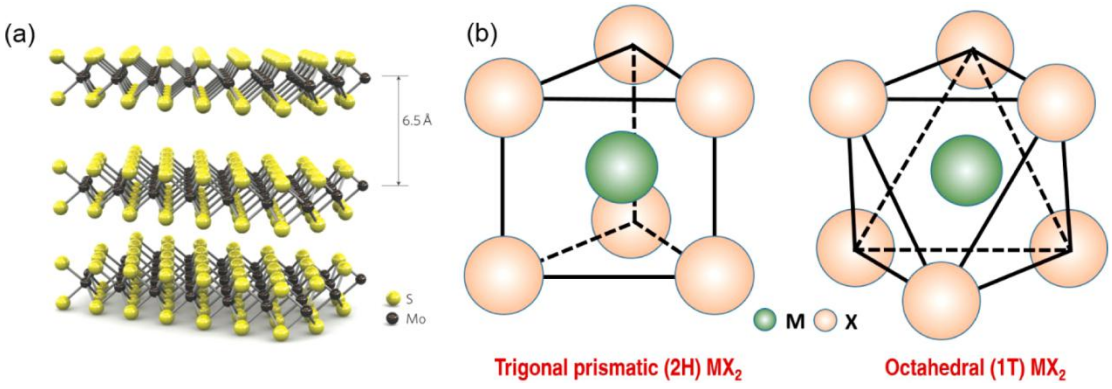

Figure 1-3. Structures of TMDs with a typical formula of MX_2. (a) Model of the MoS_2 crystal structure. (b) Unit cells of 2H-$MX_2$and 1T-MX_2 [10].

1.2 Electronic and optoelectronic properties of transition metal dichalcogenides

1.2.1 Electronic structures of TMDs

TMDs such as MoX_2 and WX_2 are semiconductors, while NbX_2 and TaX_2 are metallic in few-layer form and are superconductors in bulk[11,12]. In semiconducting TMDs, there is a change from an indirect bandgap in bulk to a direct gap in monolayers and this has attracted a great amount of attention recently. For example, calculated band structures of bulk and monolayer MoS_2/WS_2 are shown in Figure1-4. The bulk indirect bandgap of MoS_2 is 1.2 eV and increases to a 1.8 eV direct bandgap in monolayer at the K point. For WS_2 the indirect bandgap of 1.3 eV in the bulk increases to a direct bandgap of 2.1 eV in monolayers[11]. The direct bandgap has important implications in optoelectronic applications because it results in photoluminescence(PL) in monolayer MoS_2 and WS_2. It is also found that in monolayer MoS_2 the valence bands was split due to the broken inversion symmetry[13], and such spin splitting is not found in bilayer MoS_2[13].

The band structure is dependent on the layer number due to quantum confinement. The conduction band at the K-point consists of localized d orbitals of Mo atoms. These atoms lie in the middle of the sandwich S–Mo–S structure and are hardly affected by the inter-layer van der Waals forces. However, the states at the Γ-point are due to hybridization of the S atom p_z-orbitals and the d orbitals of the Mo atoms which is affected by inter-layer coupling[14]. As a result, when the layer number changes the tuned inter-layer forces affect the states at the Γ-point rather than those at the K point. Therefore there's little change in the gap near the K-point, but the gap near the Γ-point shifts a lot.

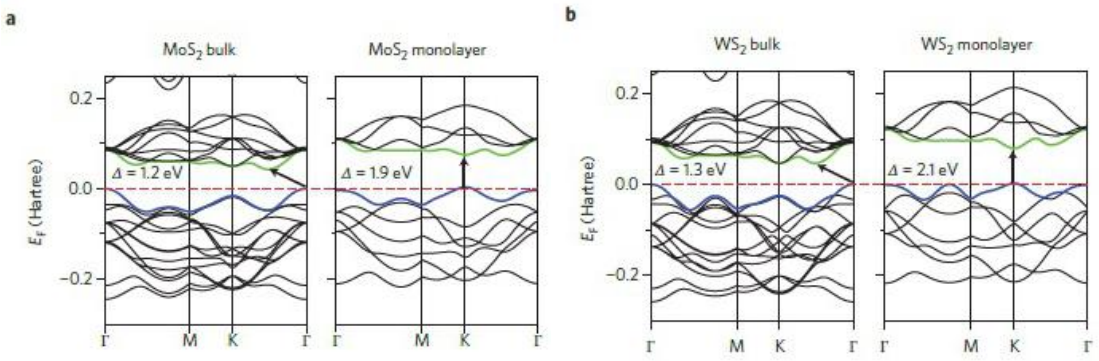

Figure 1-4. Band structures of bulk and monolayer MoS_2 (a) and WS_2 (b) calculated from density functional theory (DFT)[11]. The arrows indicate the bandgap (direct or indirect). The blue line indicates the top of the valence band and the green line indicates the bottom of the conduction band.

1.2.2 Optical properties of TMDs

The electronic band structures of TMDs have impacts on their optical properties. The direct band-gap in monolayer means that the electrons and the holes have the same momentum and thus the they can recombine easily emitting photons, results in extraordinarily strong photoluminescence for monolayer MoS_2 and WS_2[15].

Figure 1-5 shows PL of WS_2 with different layers. For monolayer, the PL is very intense and exhibits one peak corresponding to a direct band gap of 2.1 eV. For two or more layers, the indirect transition near the Γ-point starts to compete with the direct transition. The competition remarkably reduces the PL quantum efficiency. Also, a new peak appears at longer wavelengths, which is labeled I in Figure 1-5. Moreover, for 2L and 3L WS_2, there is a valence band splitting at the K point generating two distinct excitons: exciton A and exciton B[15].

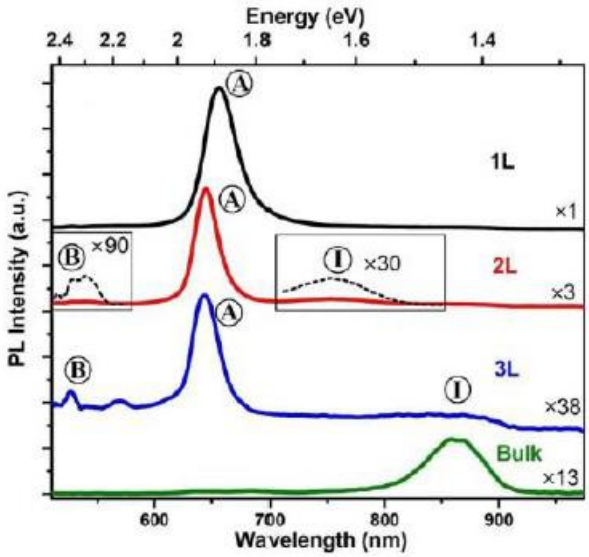

Figure 1-5. Photoluminescence for 1L, 2L, 3L, and bulk WS_2 under 488 nm excitation. The peaks for excitons A and B and also the indirect band gap (I) are labeled.

1.2.3 Vibrational properties of TMDs

The phonon modes of materials can be reflected via Raman spectra measurement. The main Raman peaks of MoS_2 contains in-plane modes: E^1_{2g} and E_{1u}, and out-of-plane mode: A_{1g}, which are shown in Figure 1-6[16]. The interaction between neighboring layers change the effective restoring forces and create a dielectric screening effect between atoms[16]. This causes a shift in the frequency of the Raman modes when increasing the number of layers (Figure 1-7a). The frequency of A_{1g} monotonically decreases, while the frequency of E^1_{2g}increases with the number

of layers. These shifts in peak position provide possibilities to identify layer thicknesses via Raman spectroscopy (Figure 1-7b).

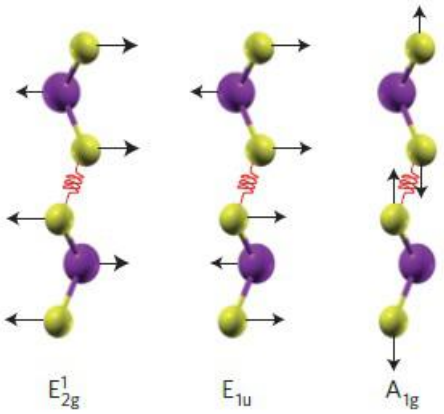

Figure 1-6. Schematic illustration of E^1_{2g} and E_{1u} modes (in plane), and the A_{1g} mode (out-of-plane) in bulk MoS_2 and WS_2[16].

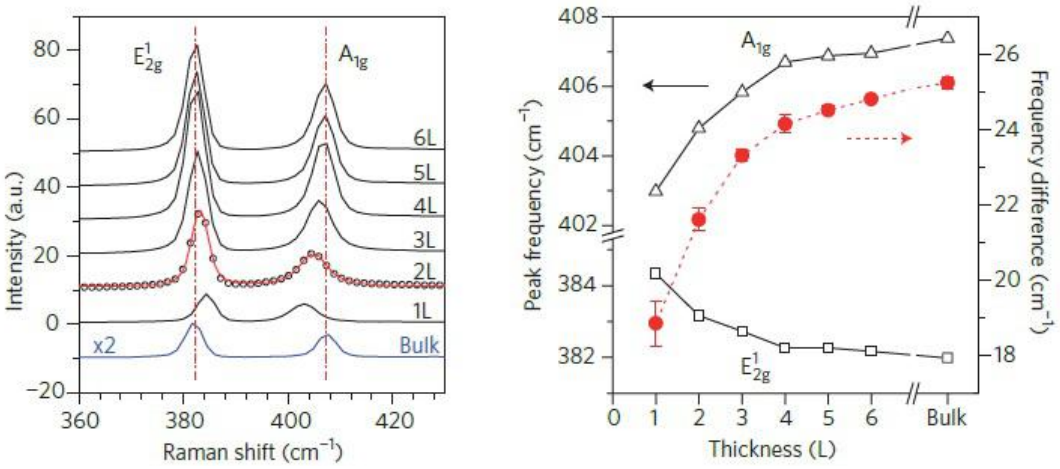

Figure 1-7. a) Raman spectra shift in frequency for MoS_2 of different thickness. b) Relationship between peak position shifts and layer thickness of MoS_2[17].

For WS_2 there are also peak position shifts for modes E^1_{2g} and A_{1g} under a 488nm excitation which are similar to MoS_2. However, for monolayer WS_2 under a 514.5 nm laser excitation, many second-order peaks that are very weak under 488 nm excitation and in the bulk form appear which are shown in Fig.8[15]. These second-order Raman resonance modes result from

a coupling effect between the electronic band and lattice vibrations, which are similar to sound waves[15]. The strongest second order Raman peak is at 352 cm^{-1}, which is identified as the 2LA(M) mode. The intensity of 2LA(M) is approximately twice as intense than that of the A_{1g}. The intensity ratio I_{2LA}/I_{A1g} is larger than 2 only when the WS_2 is single-layer[15] providing an accurate and nondestructive approach to distinguish monolayer WS_2 from few-layer or bulk WS_2.

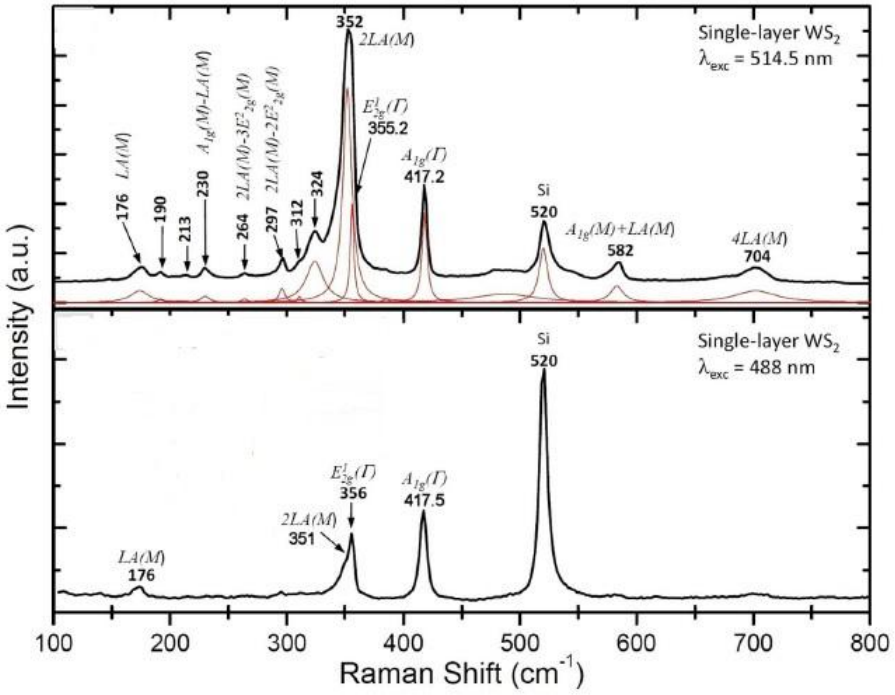

Figure 1-8. Raman spectra of WS_2 monolayer under 514.5 nm (up) and 488 nm (bottom) laser excitation[15]. The Raman modes and their positions are labeled on top of the peaks.

1.3 Van der Waals solids

As graphene has been studied during the last decade, now researchers have begun to pay more attention to other graphene-like atomically thin two dimensional materials such as hexagonal boron nitride (hBN), TMDCs and other layered oxides such as V_2O_5[18]. As well as the graphene-like materials, another topic in 2D materials field has recently emerged over the past two years [19]. This topic deals with heterostructures of different two dimensional materials

constructed by stacking different kinds of layers on top of one another. The artificial stack can assemble one-atomic-thin blocks with complicated compositions in a desired chosen sequence and structure (Figure 1-9) [20]. The layer-by-layer stacked heterostructures are covalently bonded in-plane whereas adjacent layers are relatively weakly bonded by van der Waals forces. The stability of van der Waals heterostructure has been demonstrated experimentally [21-23] as well as novel properties which exceed any of the components. The van der Waals heterostructures are expected to possess the outstanding properties of the monolayers, and at the same time, they may have new properties that can not be found in those monolayers. Therefore, studies on various van der Waals heterostructures have been conducted, looking forward to their future applications in novel electronic and optoelectronic devices.

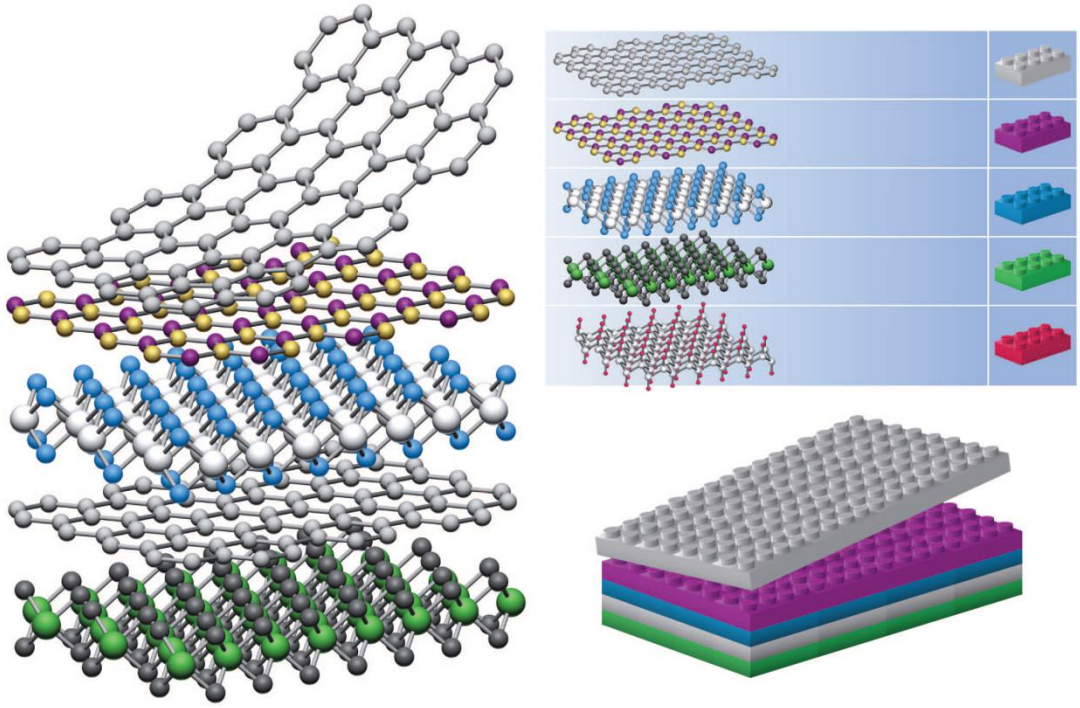

Figure 1-9. Schematic illustration of the structure of heterostructures by stacking of different 2D layered materials . Every layer of 2D material is analogous to Lego blocks, making it possible to construct a variety of layered structures[20].

Various approaches for synthesizing 2D heterostructures structures have been reported. The transfer of exfoliated layers can be employed to produce high-quality stacks[23,24]. Multi-step chemical vapor deposition (CVD) growth can synthesize multi-layer heterostructures on the proper substrate for scalable stacks [22-24]. Assembling after liquid exfoliation can produce 2D stacks in a considerable quantity. Heteroepitaxial growth can create stacked layers by growing a material on a 2D substrate such as graphene [24].

Because of the strong electron-hole confinement, extreme bendability, and the high transparency, 2D materials have attracted much attention for both fundamental research and in practical applications. In addition to the research on individual graphene-like 2D materials, plenty of effort has also been focused on hybrid heterostructures and devices of 2D materials. Creating artificial heterostructures via stacking different 2D crystals on top of each other establishes a whole family of new materials with unusual characteristics and exciting possibilities for novel 2D devices which show potential in the fields of electronic and optoelectronic devices [24].

1.3.1 Charge transfer in heterojunction

When two semiconductors with unequal band gaps are joined, a heterojunction is formed. To study the mechanism of the heterojunction and the effects of the interface is the basis of research on heterostructures. It is found that the properties of semiconductor junctions are dominated by the band alignment at the interface. Depending on the alignment of band structures, semiconductor heterojunctions can be divided into type I, type II and type III, as is shown in the Figure 1-10 respectively. In type I heterojunction, the band gap of one material is straddled by the other one, and in type II heterojunction, the band gap of the two materials are staggered, while in type III heterojunction, the band gaps do not intersect with each other.

The band offsets in the conduction band and valence band provide driving forces for charge carriers to transfer across the interface. In type II heterojunctions, the lowest energy state for holes and electrons reside on opposite sides, thus charge separation occurs when they are photo-induced. It has been suggested that type II semiconductor heterojunctions could be working as photocatalysts which can be used for solar water splitting.

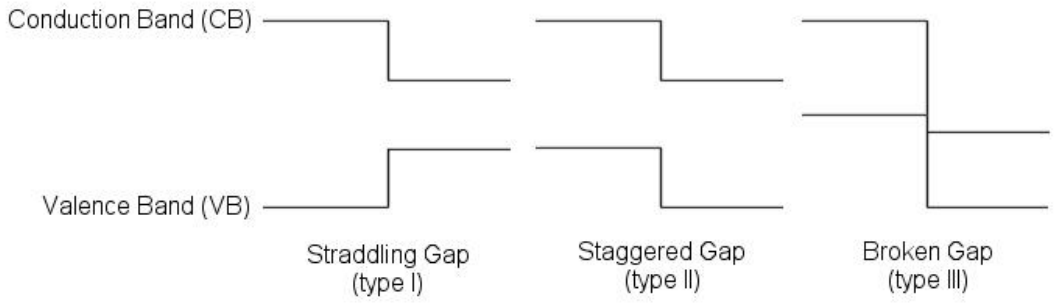

Figure 1-10. Three different alignment of band structures at the heterojunction interfaces. Type I: straddling gap; Type II: staggered gap; Type III: broken gap.

In TMD heterostructures, there are mismatchs of band structures at the interfaces between different layers. TMD heterostructures are predicted to have the type II heterojunction interface [25] in which photoexcited electrons and holes are separated by different layers.

The nature of the type II heterojuction provides possibilities of band engineering of TMD layered materials via changing the carrier density. It has been proved experimentally that optical properties of monolayer TMDs can be tuned by covering the surface with p-type dopants or n-type dopants [26]. The photoluminescence of single layer MoS_2 results from the recombination of electron - hole pairs as well as trions, which consists of two electrons and one hole. When in contact with p - type dopants, the exciton peak dominates, while the trion peak dominates when 1L MoS_2 is in contact with n - type dopants, as is shown in the Figure 1-11 [26]. Apart from the spectral weight of the exciton and trion peaks, the overall PL intensity is also affected. When the MoS_2 is p - doped, the PL intensity is drastically enhanced, and when it is n - doped, the PL is

quenched. Similar to MoS_2, the single layer WS_2 is also found to show opposite behaviors when n - doped and p - doped [27]. These behaviors are significant in the study of TMD heterostructures due to the charge separation in the type II heterojunctions.

Figure 1-12 (a) illustrates the alignment of the band structure of the heterojunction formed by MoS_2 and WS_2 monolayers [28]. It shows that the MoS_2 valence band maximum and conduction band minimum are both lower than that of WS_2, therefore, in the heterostructure, electrons accumulate in the MoS_2 layer and the holes will accumulate in the WS_2 layer. Figure 1-12 (b) shows the photoluminescence spectra of the 1L MoS_2, 1L WS_2, and MoS_2/WS_2 heterostructure. The light emission in both layers is quenched compared to the single layered MX_2, which can be explained by the charge transfer [28]. The electrons and the holes are separated by two layers, and the efficient pathway for electron - hole recombination is blocked, resulting in the quenching of PL intensity. The charge transfer is also found to be very fast, taking place within 50 fs after excitation which is promising for novel devices in optoelectronics[28].

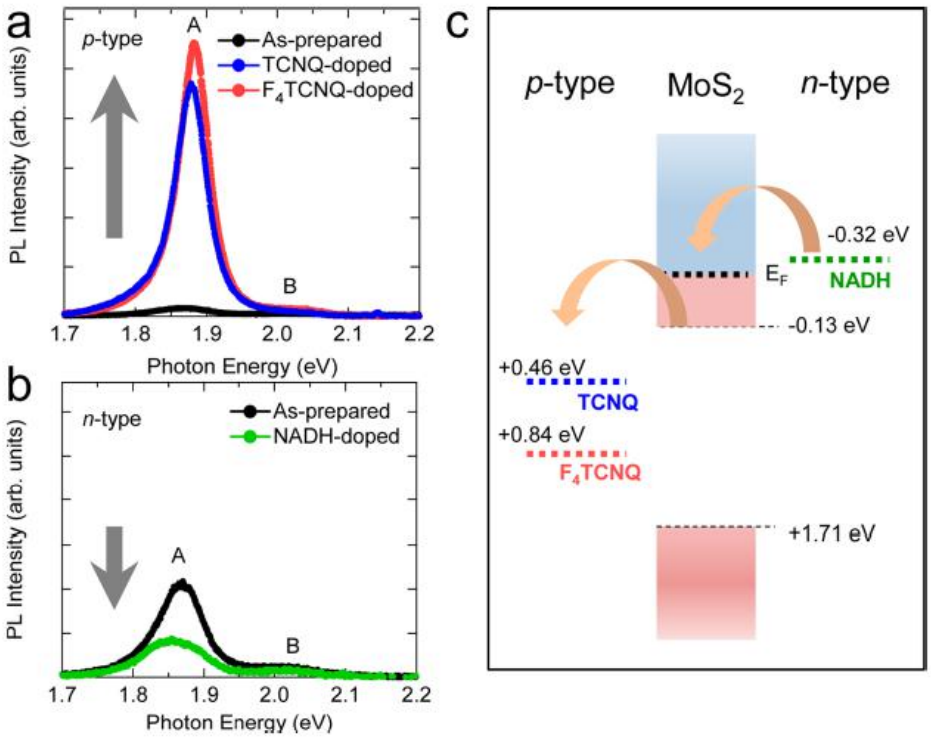

Figure 1-11. (a) Photoluminescence of single layer MoS_2 as prepared and in contact with p - type dopants; (b) Photoluminescence of single layer MoS_2 as prepared and in contact with n - type dopants; (c) Potentials of single layer MoS_2 and the dopants [26].

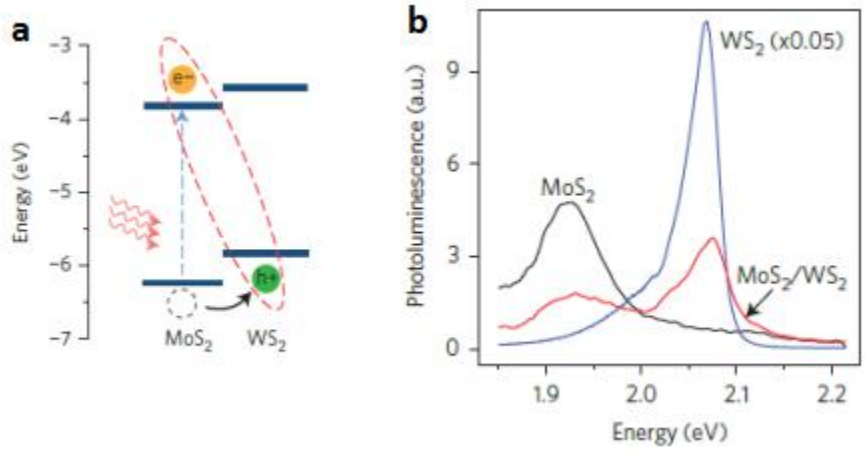

Figure 1-12. (a) Band alignment of the MoS_2/WS_2 heterostructure. (b) Photoluminescence of monolayer MoS_2, monolayer WS_2 and the MoS_2/WS_2 heterostructure [28].

1.3.2 Layer-breathing Mode - a method to characterize the vdW forces

Owing to the van der Waals bonding between stacked TMD heterostructures, new phonon modes which don't appear in single layer TMDs can be observed. These intriguing phonon modes appear in the low - frequency area since van der Waals forces have much lower bonding energy than covalent intralayer bonding. Generally, they can be divided into layer-breathing modes (LBM) and shear modes (SM), which are attributed to the out-of-plane and in-plane displacement under the interaction with the adjacent layer respectively [29-32]. Figure 1-13 gives a brief illustration of the LBM and SM phonon modes. These phonon modes are sensitive to the interface environment which includes layer thickness, stacking order, and the contact quality[33] of the 2D heterostructures. Therefore the LBM and SM modes provide methods to probe the interface of TMD heterostructures.

There have been experimental results confirming the existence of low-frequency phonon modes in TMD heterostructures as well as homostructures [33]. LBM modes are found in bilayer pristine TMDs, such as bilayer MoS_2 and WS_2, or TMD heterostructures, such as $MoSe_2/MoS_2$. Moreover, LBM modes can also be found in twisted heterostructures and homostructures for all stacking orientations, and the LBM peaks locate between 25 cm^{-1} to 40 cm^{-1} [33]. However, SM phonon modes can not be found in all cases: in pristine bilayers and the as-grown MoS_2/WS_2 heterostructures, the SM modes at around 18 cm^{-1} are active, but in twisted bilayers and some other heterostructures they are not active, which are described in Figure 1-13. The LBM peaks have higher energy and are also broader than the SM peaks [33].

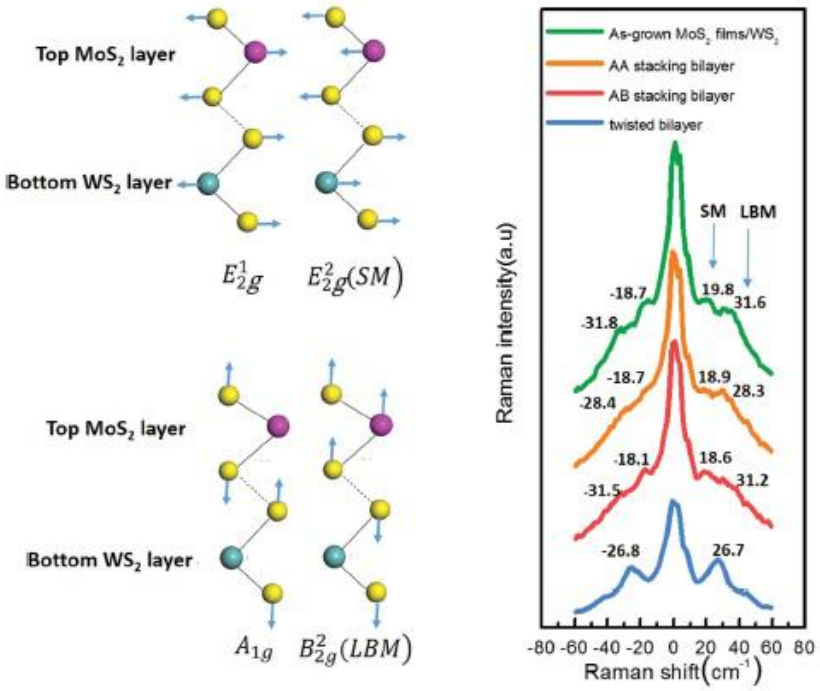

Figure 1-13. Schematic illustration of the MoS_2/WS_2 structure and low frequency phonon modes for the heterostructure (left). Low frequency Raman spectra of the as-grown MoS_2/WS_2 heterostructure, A−A and A−B stacking MoS_2/WS_2 by transfer, and twisted stacking MoS_2/WS_2 by transfer, respectively (right) [34].

The observations can be understood by considering the lattice commensuration of the heterostructure or homostructure. MoS_2 and WS_2 monolayers have very small lattice mismatch so that the heterostructure can have commensurate stacking if there are A-A or A-B stacked. When the lattices are randomly orientated, they are incommensurate. Hence, lateral displacement in the two layers can not provide a restoring force [33, 34]. Therefore the SM mode does not show up. For heterostructures with large lattice parameter mismatch, for example, MoS_2 and $MoSe_2$, even though they are Bernal stacked, their lattices are incommensurate and the SM mode is inactive in the heterostructure. In contrast, the inter-layer van der Waals forces can provide vertical restoring forces which results in the LBM vibrational modes. Van der Waals forces depend on the interlayer distance and the polarizability of the materials, therefore the LBM modes can be used

to probe the inter-layer distance, while the SM modes provide a possibility to study the crystallographic alignment [33].

References

1. L. D. Landau, Theory of phase transformations. I, Phys. Z. Sowjetunion 1937, 11, 26.

2. K. S. Novoselov, A. K. Geim, S. V. Morozov, D. Jiang, et al, Electric Field Effect in Atomically Thin Carbon Films, Science 2004, 306, 666.

3. M. J. Allen, V. C. Tung, R. B. Kaner. Honeycomb Carbon: A Review of Graphene, Chem. Rev. 2010, 110, 132–145.

4. X. Jia, J. C. Delgado, M. Terrones, V. Meunier and M. S. Dresselhaus. Graphene edges: a review of their fabrication and characterization, Nanoscale, 2011, 3, 86–95.

5. A. K. Geim, K. S. Novoselov. The rise of graphene, Nature materials, 2007, 6, 183-191.

6. A. H. Castro Neto, F. Guinea, and N. M. R. Peres, Drawing conclusions from graphene, Phys. World 2006, 19, 33-37.

7. L. Song, L. Ci, H. Lu, et al, Large scale growth and characterization of atomic hexagonal boron nitride layers, Nano Lett. 2010, 10, 3209–3215.

8. D. Pacile, J. C. Meyer, C. O. Girit, A. Zettl, The two-dimensional phase of boron nitride: few-atomic-layer sheets and suspended membranes. Appl. Phys. Lett. 2008, 92, 133107.

9. Y. Lin and J. W. Connell. Advances in 2D boron nitride nanostructures: nanosheets, nanoribbons, nanomeshes, and hybrids with graphene, Nanoscale, 2012, 4, 6908–6939.

10. R. Lv, J. A. Robinson, R. E. Schaak, D. Sun, Y. Sun, T. E. Mallouk, and M. Terrones. Transition metal dichalcogenides and beyond: synthesis, properties, and applications of single- and few-layer nanosheets, Acc. Chem. Res. 2015, 48, 56−64.

11. A. Kuc, N. Zibouche, T. Heine, Influence of quantum confinement on the electronic structure of the transition metal sulfide TS_2, Phys. Rev. B 2011, 83, 245213.

12. Q. H. Wang, K. Kalantar-Zadeh, A. Kis, J. N. Coleman, M. S. Strano. Electronics and optoelectronics of two-dimensional transition metal dichalcogenides, Nature nanotechnology 2012, 7, 699-712.

13. K. F. Mak, K. He, J. Shan, T. F.Heinz, , Control of valley polarization in monolayer MoS_2 by optical helicity, Nature Nanotech. 2012, 7, 494–498.

14. K. F. Mak, C. Lee, J. Hone, J. Shan, T. F. Heinz, Atomically thin MoS2: a new direct-gap semiconductor. Phys. Rev. Lett. 2010, 105, 136805.

15. H. R. Gutiérrez, N. Perea-López, A. L. Elías, A. Berkdemir, B.Wang, R. Lv, F. López-Urías, V. H. Crespi, H. Terrones, and M. Terrones. Extraordinary Room-Temperature Photoluminescence in Triangular WS_2 Monolayers, Nano Lett., 2013, 13 (8), 3447–3454.

16. A. Molina-Sanchez, L. Wirtz, Phonons in single-layer and few-layer MoS_2 and WS_2, Phys. Rev. B 2011, 84, 155413.

17. C. Lee, et al. Anomalous lattice vibrations of single- and few-Layer MoS_2, ACS Nano 2010, 4, 2695–2700.

18. K. S. Novoselov, et al. A roadmap for graphene. Nature 2012, 490, 192–200.

19. C. R. Dean, et al. Boron nitride substrates for high-quality graphene electronics. Nature Nanotechnol 2010, 5, 722–726.

20. A. K. Geim, et al. Van der Waals heterostructures. Nature 2013, 499, 419-425.

21. L. A. Ponomarenko, et al. Tunable metal–insulator transition in double-layer graphene heterostructures. Nature Phys 2011, 7, 958–961.

22. L. Britnell, et al. Field-effect tunneling transistor based on vertical graphene heterostructures. Science 2012, 335, 947–950.

23. C. R. Dean, et al. Graphene based heterostructures. Solid State Commun 2012, 152, 1275–1282.

24. H. Wang, et al. Two-dimensional heterostructures: fabrication, characterization, and application. Nanoscale 2014, 6, 12250–12272.

25. H. Komsa, A. Krasheninnikov, Electronic structures and optical properties of realistic transition metal dichalcogenide heterostructures from first principles 2013, Phys. Rev. B 88, 085318.

26. S. Mouri, et al, Tunable Photoluminescence of Monolayer MoS_2 via Chemical Doping. Nano Lett. 2013, 13, 5944−5948.

27. N. Peimyoo, et al, Chemically Driven Tunable Light Emission of Charged and Neutral Excitons in Monolayer WS_2. ACS Nano, 2014, 8 (11), 11320–11329.

28. X. Hong, et al, Ultrafast charge transfer in atomically thin MoS_2/WS_2 heterostructures. Nature Nanotechnology 2014, 9, 682–686.

29. H. Zeng, B. Zhu, K. Liu, J. Fan, X. Cui, and Q. M. Zhang, Low-frequency Raman modes and electronic excitations in atomically thin MoS2 films, Phys. Rev. B 2012, 86, 241301.

30. C. H. Lui, L. M. Malard, S. Kim, G. Lantz, F. E. Laverge, R. Saito, and T. F. Heinz, Observation of Layer-Breathing Mode Vibrations in Few-Layer Graphene through Combination Raman Scattering, Nano Lett. 2012, 12, 5539.

31. Y. Zhao, X. Luo, H. Li, J. Zhang, P. T. Araujo, C. K. Gan, J.Wu, H. Zhang, S. Y. Quek, M. S. Dresselhaus, and Q. Xiong, Interlayer Breathing and Shear Modes in Few-Trilayer MoS_2 and WSe_2, Nano Lett. 2013, 13, 1007.

32. X. Zhang, W. P. Han, J. B. Wu, S. Milana, Y. Lu, Q. Q. Li, A. C. Ferrari, and P. H. Tan, Raman spectroscopy of shear and layer breathing modes in multilayer MoS_2, Phys. Rev. B 2013, 87, 115413.

33. C. H. Lui, et al. Observation of interlayer phonon modes in van der Waals heterostructures. Phys. Rev. B 2015, 91, 165403.

34. J. Zhang et al. Observation of Strong Interlayer Coupling in MoS_2/WS_2 Heterostructures, Adv. Mater. 2016, 28, 1950–1956.

Chapter 2

Transfer and Assembly of Atomically Thin Layers

2.1 Introduction to transfer technique

Due to the high temperature used in the CVD growth processes of MX_2 monolayers at 700-800 ℃ , the substrates are limited to heatproof wafers such as silicon and sapphire, temperature-sensitive substrates such as polymers can not be used in the CVD process. Moreover, the growth of MX_2 layers requires an ordered substrate structure for an epitaxial process. However, MX_2 monolayers on soft polymers or amorphous substrates are interesting in some field areas. Thus, it is essential to transfer large area MX_2 onto all kinds of substrates with little harm to the MX_2 crystal quality. There have been many transfer techniques reported, but most of them can be organized into two main types, wet transfer, and dry transfer. For wet transfer techniques, usually liquid chemicals are used to etch parts of substrates to set the MX_2 film free. It comes associated with the problems of contamination from the etchants and harm to the MX_2 crystal quality under the corrosive environments. However, the wet transfer process is easy and quick, and has little limitations when compared to dry transfer (see below). Therefore, the wet transfer techniques are more widely used than the dry transfer.

In contrast to the chemical-driven wet transfer, dry transfers are driven by physical forces only. Usually, a stick-and-peel ‘stamp’ process is taken, requiring controls over the adhesion forces between the sample and the substrates. The polymer chosen to peel the sample should be adhesive enough to separate the sample from the substrate, and also the polymer should be soluble in water or alcohols. The process is clean when compared to the wet transfer and can

avoid the wrinkles introduced by chemically transfer, thus the dry transfer can preserve the high-crystalline quality of MX_2 monolayers during transfer. However, there are still drawbacks of dry transfers. Because the dry transfers are based on mechanical forces, the polymer-sample interaction must be very strong, therefore it has more requirements on the materials for transfer. To be more specific, the sample for transfer must consist of isolated flakes, uniform in thickness, and clean from growth reactant residues. Variations in thickness will reduce the adhesion forces between sample and polymer, and result in failure of peeling off. Unlike the exfoliated flakes, for most CVD samples dry transfers are not suitable. Therefore, dry transfers are widely used in exfoliated graphene, h-BN, and TMD flakes, and wet transfer techniques are more common in CVD grown 2D materials.

In this chapter, we will show the details of the transfer processes and discuss how different procedures during the transfer can influence its quality. Then we will discuss the transfer results and characterizations of the transferred samples. The study of transfer's effects on the samples will be helpful in the discussions of heterostructure properties in the following chapter. Finally, we will summarize on the transfer results and challenges associated to the transfer of MX_2 samples.

2.2 Wet chemical transfer

Although most of the wet transfer procedures look similar, there are some modifications depending on the particular situation. Here, an overview of our steps of transferring is given and how the procedure is modified in some specific situations is also discussed.

2.2.1 Preparation

The raw samples of layered TMD crystals for stacking are usually prepared by mechanical exfoliation from the bulk single crystals and chemical vapour deposition (CVD). In our works, all of the samples are grown on SiO_2/Si wafers or sapphire wafers via the CVD method. In the CVD process there might be some unreacted powder precursors so that cleaning before starting the transfer process is mandatory. As grown samples are sonicated in acetone for 10 seconds. In this cleaning step, only acetone can be used because other frequently used solvents such as water and isopropyl alcohol are polar molecules and will lead to degradation of TMD thin layers. After sonication, the wafers are dried under ultra-high-purity N_2 flow slowly at room temperature. For exfoliated 2D layers, sonication is not suggested because the affinity between the wafer and the mechanically exfoliated materials is rather weak compared to the CVD grown samples and the crystals might be flushed away from the wafers during sonication. Fortunately, exfoliated samples can be clean as long as every step is conducted correctly during exfoliations, and N_2 flow at 200 sccm at room temperature is enough for exfoliated samples.

2.2.2 Spin coating supporting films

High-quality 2D crystals are usually very small, between 10 - 50 microns with thicknesses around 1 nm. Therefore a supporting film is needed in the transfer process to act as a medium to peel the atomically thin layers off of their original substrate and to protect the samples from being broken. The desired materials for making the film must be flexible for holding the flakes and strong so that it will not crack during transfer. Moreover, high transparency would be preferred so that the flakes can be found under an optical microscope. Finally, the film material needs to be easily dissolved by some solvents without damaging the sample. Considering all of

the requirements, one of the most frequently used supporting material is Poly-methyl methacrylate (PMMA), a thermoplastic polymer material which can be easily dissolved in acetone. The polymer is introduced by spin-coating and the thickness of the layer can be controlled by the spin speed. Thus we can design the strength of the film-the higher thickness of the polymer film, the higher strength. We are using 495PMMA A solution and 950PMMA A solution. 495 and 950 mean the weight of the polymer molecules, A means the polymer is dissolved in anisole. Figure 2-1 shows the relationship between the thickness and the spin speed in different PMMA solutions.

With the thickness and spin speed curves, we can easily optimize the thickness of the PMMA supporting films. However, the optimization depends on different situations. Generally, we find that PMMA films work well with a thickness around 400nm, it is transparent to allow the observation of flakes under microscopes and it is strong enough for surviving every step in the wet transfer process. For 950PMMA A6 a spin speed of 3000rpm would be chosen for the supporting film. There are also some cases that we want a very thin supporting film, for example, to transfer samples onto a tiny grid for TEM, 495PMMA A3 and 2000 rpm spin speed are applied to introduce a 200nm-thick supporting film.

After spin coating, the sample with the coating is baked on a 150℃ hotplate for 2 hours to cure. When the film is cured completely and cooled down, the sample is almost ready for etching. There are two things that we can do now to improve the quality of transfers: remove the PMMA coatings on the lateral sides of wafers with a blade, and observe the location of the target flakes on the wafer and cut the useless parts of the wafer carefully. In order to remove the PMMA coatings on the lateral sides it is necessary to expose the SiO_2 layer to the etchant so it can react quickly. To cut the useless parts of the wafer one can scale down the size of the film we want to transfer, which will reduce the duration time of etching, minimizing the damage to the flakes.

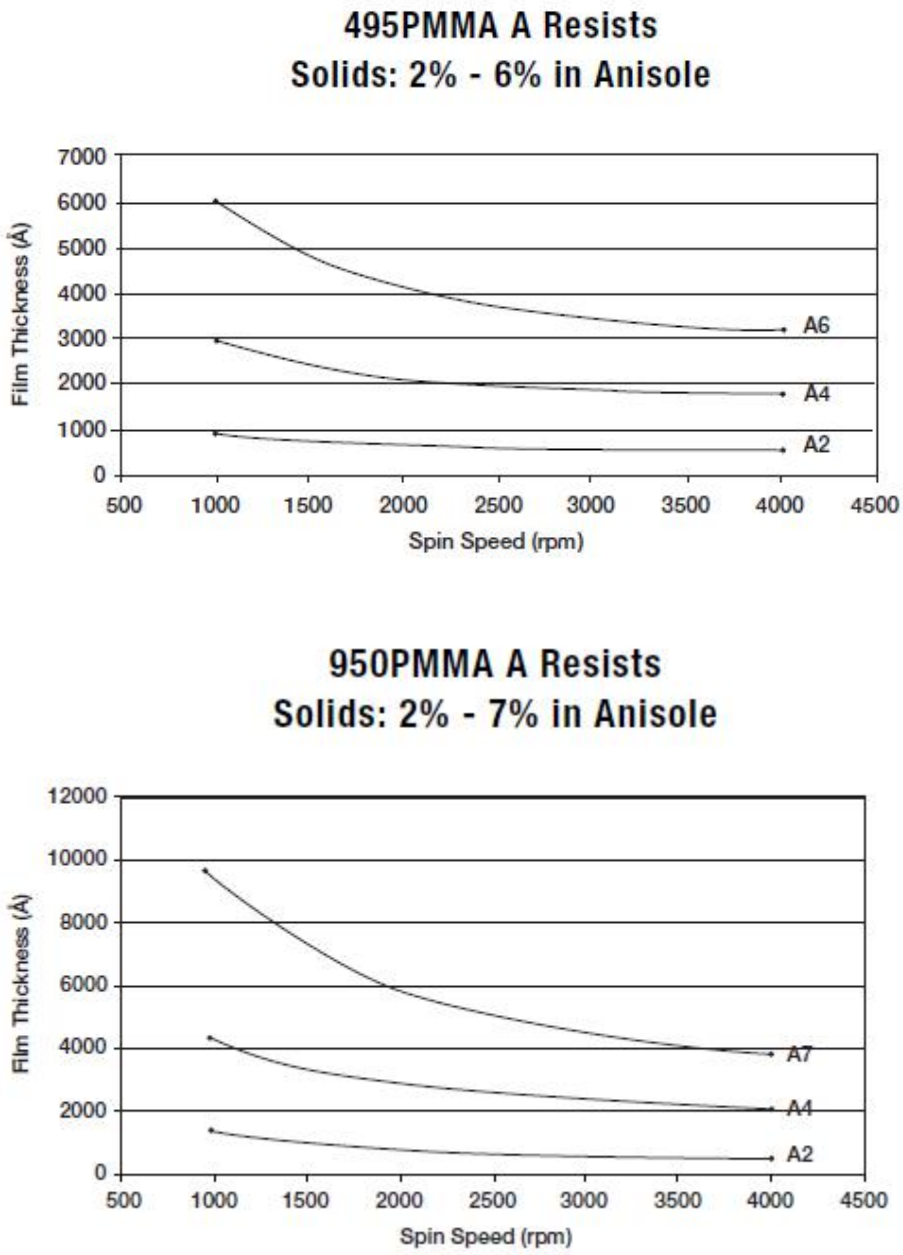

Figure 2-1. Control of 495 PMMA and 950 PMMA film thickness by spin speed. Each curve represents a solution of PMMA, i.e., A2 refers to PMMA solution in anisole with a concentration of 2%.

2.2.3 Releasing the film

The releasing of the flakes from the substrate is realized by etching the SiO_2 layer between the 2D flakes and Si wafer, so that the 2D material is isolated and get incorporate in the PMMA film. Since PMMA is hydrophobic, the film holding the flakes will float on the solution surface while the Si wafer sinks to the bottom of the container. In this step, the etchant should be able to etch SiO_2 without producing any insoluble resultants. Therefore, NaOH, KOH, and HF are good for etching. NaOH and KOH are commonly used for that because they are safer and more convenient to use and provide a mild condition during etching. NaOH and KOH etchants work at 80℃ and will take a few minutes to release the film. HF is toxic and extremely reactive compared to the base ethants and takes only one second to etch so that HF is seldom used except for some special samples. For instance, samples which are very difficult to remove and to etch, samples which require very fast etching, and samples which are grown on sapphire. The etchant should be chosen according to the sample, however, the base etchants are preffered.

No matter how the film is released, it should be rinsed with deionized water 3 - 6 times to remove the residue of the etchant. After etching the film is transferred to target substrates or micromanipulators for determinstic transfer, which will be performed in the next section.

2.2.4 Deterministic transfer

Deterministic transfer is needed when transferring flakes to the desired position in devices and stacking heterostructures in a vertical direction. Precise control of the position and orientation of the transfer process is important. Deterministic transfer can offer better control of deposition position and orientation compared to the traditional wet chemical transfer.

After the film is released and rinsed by DI water, the flakes can be transferred to a

micromanipulator and located under an optical microscope and deposited precisely at the position of interest on the target substrate. Subsequently, the polymer layer is removed, leaving the TMD layer transferred to the desired position. A schematic illustration of the deterministic transfer set up is shown in Figure 2-2 (upper). Figure 2-2 (bottom) shows a transferred bilayer MoS_2 triangle on the electrode via deterministic transfer method.

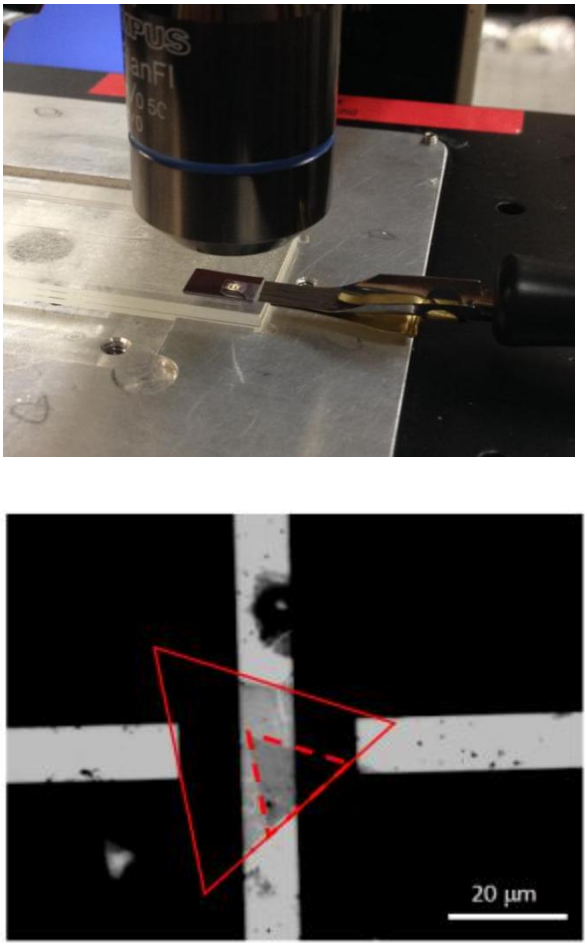

Figure 2-2. Schematic illustration of the deterministic transfer set up (upper) and transferred bilayer triangle on the electrode via deterministic transfer method (bottom). The red line shows the edges of the triangle, while the dashed red line indicates the bilayer area, which is located on the electrode via deterministic transfer.

2.2.5 Removal of PMMA

Finally, the film of PMMA needs to be removed after the transfer methods. The transferred sample is dried for 30 minutes at room temperature so that the sample can adhere to the new substrate. Then it is rinsed by pure acetone to dissolve the PMMA and is ready for most of the characterizations.

Although most of the PMMA can be removed by acetone, there can still be nano-scale PMMA residues remaining on the surface of samples. The residues won't affect the optical properties of the 2D materials, but it will affect some atomic scale characterizations such as TEM and AFM. Moreover, if we want to stack a well-coupled heterstructure, the residue is a problem. In these cases, post annealing is required for transferred samples. The sample is annealed at 300℃ for 4 hours in a mixture of nitrogen and 15% hydrogen atmosphere at 10 torr. Annealing procedure will influence the properties of 2D materials, especially for heterostructures, and will be discussed in a later section.

In conclusion, the wet transfer method is easy to perform, and it is commonly used for transferring 2D materials. The problems that come with wet transfers include a high chance of contamination, strain introduced to the sample during the releasing process, and sometimes etchants damage the samples. In order to improve the crystalline quality of the transferred sample, we can try to apply milder environment to the transfer process, which means lower temperature, shorter time, and less harmful chemicals. We can also anneal the sample at 300℃ under low pressure to recover the properties of 2D samples. If a very high crystalline quality of the 2D flakes is required, using dry transfer would be recommended. Dry transfers are more complex and can have a very different procedure for different samples. We will discuss a general procedure of dry transfer below.

2.3 Dry transfer procedure

The preparation for the dry transfer method is similar to the wet transfer, the samples also need to be spin coated with supporting films. The supporting films of dry transfer vary a lot for different samples because they are required to have not only strength and transparency but also adhesive forces to peel off the flakes. Usually, the more layers of the flakes, the more adhesive the polymer needs to be. An example of a supporting polymer for dry transfer is polyvinylpyrrolidone (PVP) with poly(vinylalcohol) (PVA)[1], both of which are water soluble polymers. Firstly, the PVP film is spin coated onto the sample. The PVP polymer has strong adhesion and wetting capability so that it is an adhesive layer to ensure 2D flakes can be peeled off [1]. However, the PVP film lacks flexibility and may break while peeling, so that the next step is to spin coat a supporting layer- the PVA film. The combination of PVP and PVA provides both strong adhesion force and strength. Using both films, 2D flakes can be peeled off from the original substrate[1]. Usually, different types of 2D materials require different adhesive force, and the concentration of PVP should be adjusted to provide the best adhesion. For monolayers, the concentration would be lower, and for multilayers, it should be higher. Finally, the polymers are dissolved in warm DI water. Compared to the wet transfer method, it avoids contamination from the etchants and wrinkles on samples after transfer. However in some cases, the interaction between the flakes and substrates is so strong that it is very difficult to peel off by adhesive forces.

There is also another transfer technique which is achieved by simply sonication which is named ‘bubbling’ transfer method [6]. The first step of this method is also introducing a layer of a supporting polymer film, similar to the wet chemical transfer method. After curing the polymer film, the film with the sample is released from the substrate via ultrasonication in deionized water. One minute is needed to separate them, and the film will be floating on the surface of the water. This method can be regarded as a combination of the wet transfer method and the dry transfer

method. It is conducted in the wet environment, but there is no chemical etchant involved, in other words, it is a physical process. It is the most convenient method, and the damage to the sample after the transfer is limited since the use of chemicals is avoided. However, not all of the TMDC sample can be successfully released by this method.

2.4 Influence on TMD monolayers after transfer

As is mentioned in the previous sections, the transfer process affects the crystalline quality of the 2D flakes depending on the transfer method, the type of sample, the target substrate, as well as some other factors. In our study of TMD heterostructures, the transfer method is applied to artificially stack monolayers. In this section, we will compare some physical and chemical properties of TMD monolayers before and after transfer on different substrates.

2.4.1 Optical microscope

The optical microscope is a useful technique for rough inspection of properties of the TMD monolayers before using more precise instruments such as Raman spectroscopy, photoluminescence, AFM etc. According to the uniformity and the color of samples under an optical microscope, we can know about the quality and also the thickness of the samples.

All of our TMD monolayer samples are synthesized by the CVD method and then transferred by the wet chemical method. Optical images of the samples before transfer and after transfer are shown in Figure 2-3. All of the images are taken at 50X magnification. For all of the original and transferred samples, the optical images provide good contrast and show clearly the shape of the triangles, which means that the crystal structure of the samples is well preserved after transfer. The flakes are adhered to the new substrates very well, even on the curved surface.

However, the contrast of the samples looks slightly different on different substrates. In the image of the original samples (Figure 2-3 a), we can find a darker triangular area in the center of the crystal. This is because the crystallization starts from the center during the CVD process leading to a multilayer area (typically 2-3 layers) in the center. The contrast remains the same in the image of transferred sample on the SiO_2/Si wafer (Figure b). When it is transferred on a transparent wafer such as sapphire (c) and glass (d), the contrast becomes opposite to that of Si wafer. The monolayer area of the triangle is slightly brighter than the substrate, and for the crystal core area, it is nearly white. On the SiO_2/Si wafer, the flakes scatter most of the incident light and the bare wafer reflects most of the incident light so that the flakes look darker than the wafer. On the transparent wafer, most of the light pass through the wafer so that the bare wafer will look very dark under the microscope so that the scattered light from the 2D flakes will make them look brighter than the substrate.

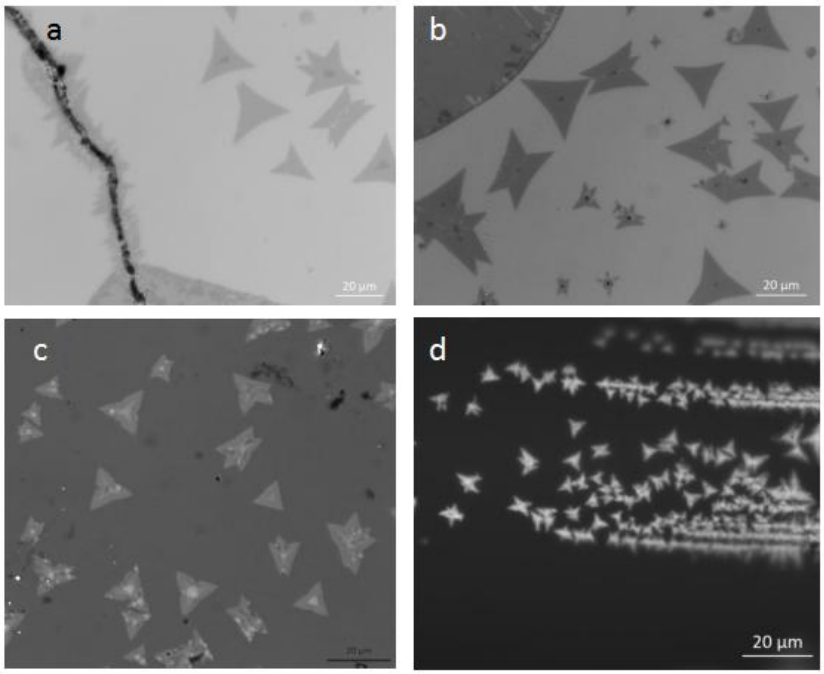

Figure 2-3. Optical image of WS_2 before and after transfer: as grown WS_2 monolayer crystals(a); transferred on the SiO_2/Si wafer(b); tranferred on the sapphire (c) and a glass fiber (d).

2.4.2 Photoluminescence of TMD monolayers

As is mentioned above, the transferred TMD monolayer triangles preserve a good structure at the micron scale under the optical microscope. However, the crystal structure at nanoscale is more important since the unique fluorescent properties of TMD monolayers rely on it. In order to inspect the microscopic quality of the transferred TMD monolayers, fluorescent microscopy and the photoluminescence spectroscopy are applied to characterize the samples before and after the wet chemical transfer.

The optical and the fluorescent images of a crystalline triangular WS_2 sample after wet chemical transfer are shown in Figure 2-4. The clear shapes of the triangles show the crystalline quality of the transferred sample. According to the different contrast in the optical images (left), it is found that most of the triangles are monolayers but there are some bilayer triangles and multi-layered areas. The number of the layers can be confirmed by comparing with the fluorescent image on the right: the monolayers have very strong fluorescence while bilayers and multilayers show no fluorescence. The fluorescence of the monolayer WS_2 triangles are intense at the edge and quenched in the center area. In the fluorescent triangles, there are three dim lines which are situated at the bisectors of the triangles. Considering the crystalline nature of the samples, the dim lines are probably the grain boundaries and therefore one triangle of WS_2 is composed of three single crystals and the orientations of the crystal domains show triple rotational symmetry. The quenching of the light emission can prove that those lines are grain boundaries because a large amount of defects and dislocations accumulated around the grain boundaries usually acts against the electron-hole recombination and thus leads to the quenching of light emission. Taken altogether, the properties of light emission of the TMD crystals remain after transfer, following the layer-number-dependent rules and the effect of grain boundaries. However, we can not figure out detailed information of the light emission quality, for example, the intensity and position of

the emission. In order to investigate the influence of the transfer process on the quality of light emission, photoluminescence is applied to the sample. Comparison of the photoluminescence of the sample before and after transfer may show the answer.

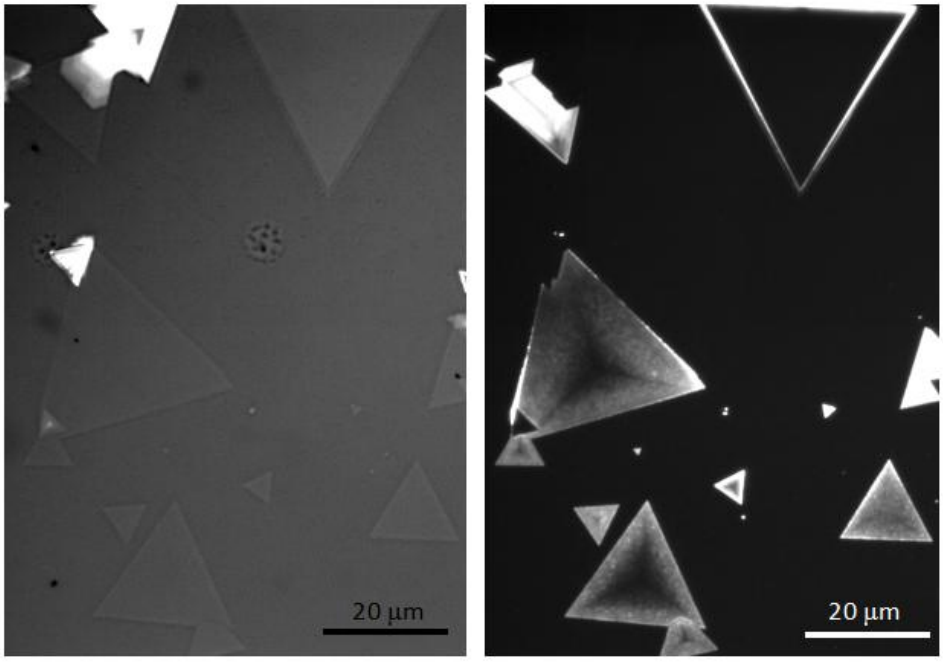

Figure 2-4. The optical image (left) and fluorescent image (right) of a crystalline WS_2 triangle sample after wet chemical transfer. The bright white color of the triangle edges indicate strong fluorescent signals.

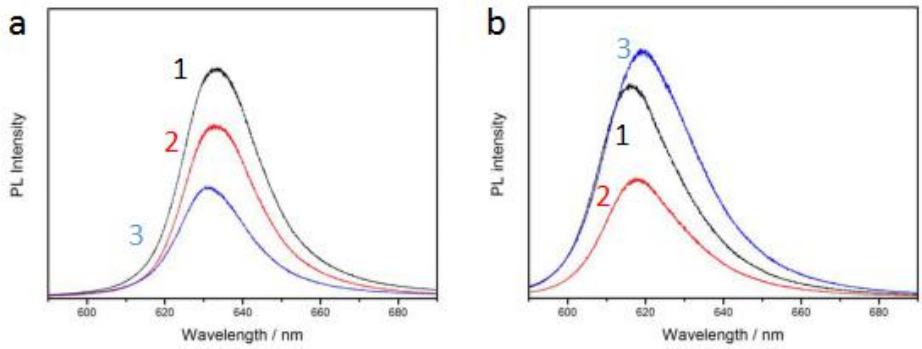

Figure 2-5. Photoluminescence of WS_2 before (a) and after wet chemical transfer (b). The black, red, and blue lines represent three different samples, respectively. The PL spectra were taken from the same spots before and after transfer.

Photoluminescence spectra were taken from three different triangles in the WS_2 sample. After the wet chemical transfer, PL spectra were conducted again at the same sample locations. The spectra of these triangles are shown in Figure 2-5 with different colors. Comparing the PL of original samples and the transferred samples, the first thing we notice is that the wavelength of the fluorescent light is blue shifted, from around 635 nm to 620 nm. The wavelength shift corresponds to 0.05 eV energy enhancement of the emitted photons. These shifts are due to the strain induced by the substrate. It has been demonstrated experimentally and theoretically that mechanical strain can disturb the band structure of MoS_2 because the band gap energy and the carrier effective masses are modified [2] as is shown in Figure 2-6.

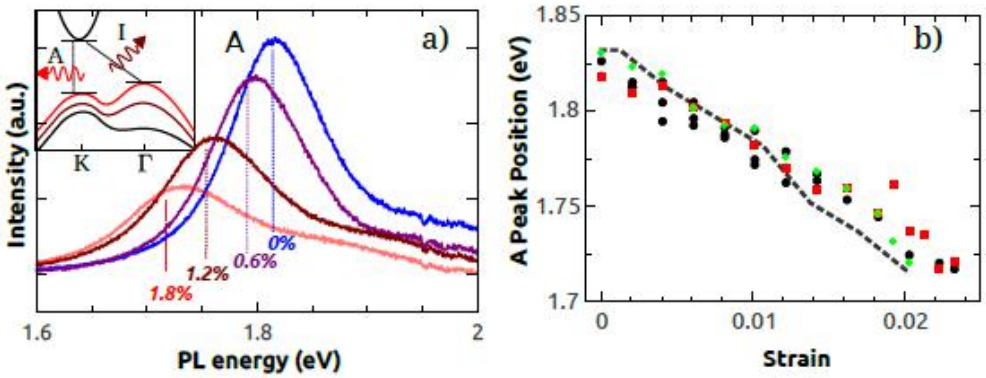

Figure 2-6. (a) Photoluminescence of strained MoS_2 monolayer from 0 to 1.8%. The insert image shows the mechanism of PL in monolayer MoS_2 materials. (b) Dependence of the position of the principle PL peak on the strain [2]. The black, red and green dots stand for three different samples.

The experimental results of the strained MoS_2 show that the position of the principle photoluminescence peak is red shifted from around 1.8 eV to 1.7 eV under 1.8% mechanical strain [2]. WS_2 and MoS_2 possess very similar crystal structure and properties so that PL of the strained WS_2 would also be red shifted. This result is consistent with our results of blue shifted PL after transfer, since the transferred WS_2 monolayer is released from the original substrate and has little interaction with the target substrate, which means that transferred WS_2 can be regarded

as a free standing layer with 0% strain. The as-grown CVD sample is bounded to the substrate, and mismatch in atomic lattice induces strain to the lattice of the WS_2 layer, therefore the PL peak is red shifted. The energy shift by strain is important in monolayer TMD band modulation and also in the study of the heterostructures because in heterostructures the strain environment is more complex.

Besides the position, the height and width of the A peak are also changed after transfer. The three curves in different colors represent three triangles from the sample. For all of them, the widths of the peaks are widened from 25 nm to 30 nm. Correspondingly, the peaks are lower in height compared with the data before transfer, although at different extents for the three triangles. The widening and lowering of the peaks probably result from the introduction of contamination and defects during the transfer. As we discussed in the previous section, the etchant NaOH may contaminate the sample, and also the chemical environment may damage the quality of the atomic structures by introducing defects. Photoluminescence of a perfect monolayer TMD crystal should be very intense and sharp. When defects and contamination come into the lattice, the defect energy levels for electrons form near the conduction band minimum, and the excited electrons are able to jump to those defect levels before recombining with the holes in the valence band. Therefore, the emitted photons are not monochromatic but include some photons with energy close to the band gap. Finally, the peak is widened and at the same time, the height of the peak is lowered. This result demonstrates that the transfer process accelerates the degradation of the TMD crystals. The damage is acceptable to our research because the shape of the primary PL peak did not change a lot, and that means that there is not too much contamination. The problem is the intensity loss after transfer, but it is still intense enough for analysis. Therefore, in our work, the wet chemical transfer method is adopted.

2.4.3 Photoluminescence of TMD on different substrate

To understand the optical properties of a transferred sample, the effect of substrates also needs to be considered as an important factor. Figure 2-7 shows the effect of the substrate by comparing the fluorescence of the layers on a Si wafer with suspended layers. The MoS_2 monolayer triangle sample is transferred onto a Si wafer with 2-micron-diameter holes. The transferred MoS_2 over the holes is not in contact with any materials and can be regarded as suspended layers. After removing the PMMA, the sample is observed under a fluorescent microscope. From the image, we can find that the suspended layers have much more intense fluorescence than the layers in contact with the substrate. The phenomenon is due to the scattering of the substrate. The substrate scattered most of the light emitted by the MoS_2 layer, and the fluorescence on the substrate is quenched, which makes the suspended layers look bright under the microscope.

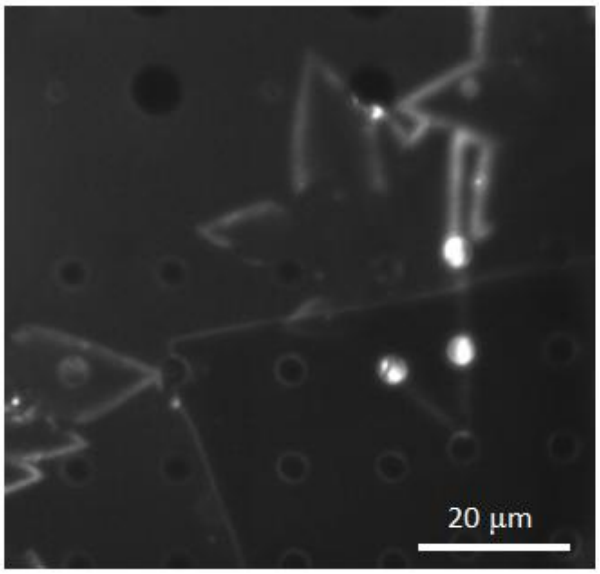

Figure 2-7. Fluorescent image of MoS_2 monolayer triangles transferred on to Si wafer with holes. The bright white color of the triangle edges indicate strong fluorescent signals of the suspended layer.

Apart from the scattering effect, different substrates can have a different impact on the light emission spectra of the TMD monolayers due to the interaction between them. Although the interaction between the sample and the substrate is weakened after transfer, the sample can be influenced by charge transfer. There have been some publications discussing the modulated PL of TMD monolayer by charge transfer. When the sample is in contact with an electron donor material, extra electrons will be injected into the conduction band of the sample and forming negative trions. In this case, the sample is n-doped. When the sample is in contact with an electron acceptor material, electrons will be extracted from the sample, and holes accumulate in the valence band of the sample, forming positive trions. In this case, the sample is p-doped.

In an undoped system, the electrons are excited to the conduction band and holes are left in the valence band. The electron-hole pair bond together by an electrostatic Coulomb force and the pair is named exciton. In a doped system, for example, n-doped system, extra electrons are introduced to the conduction band. Instead of staying isolated, the extra electrons are tightly bound to excitons. The negatively charged exciton, which is called trion, is formed by two electrons and one hole [3]. Before the recombination of the electron and the hole, the extra electron needs to be removed from the trion, as is shown in Figure 2-8. Extra energy is needed for dissociation of the trion and results in the emission of two peaks, the neutral excitons peak (usually called A) and the negatively charged trions (usually called A^-). The energy of the negatively charged trions peak is lower than the neutral excitons peak, The minimum energy for the dissociation of a trion can be determined from the energy difference between the two peaks. If the system is p-doped, then the trions would be positively charged, and the trions peak (A^+) has higher energy than the excitons peak according to the mechanism.

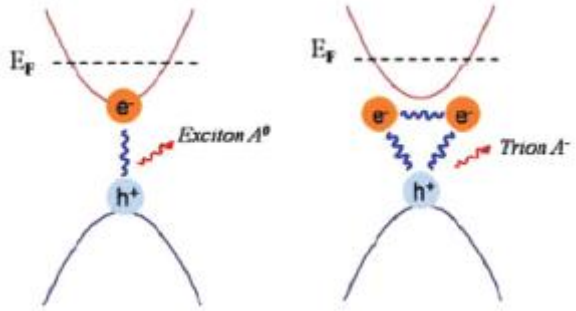

Figure 2-8. A schematic illustration of the formation of neutral excitons and negatively charged trions [3]. One electron and one hole forms a neutral exciton A^0, while two electrons and one hole form a negative trion A^-.

Charge transfer between monolayer TMD and substrates is similar to the doping process [4]. In the undoped system, the dissociation energy is simplified to the trion binding energy. However, when the system is doped, the extra electrons raise the Fermi energy and thus the dissociation energy is also increased [4]. Therefore, the weight of neutral excitons and trions can be modulated. When the monolayer TMD is in contact with different substrates, the potential to inject electrons/holes to the TMD is different, thus resulting in different doping concentration, and changing the relative intensity ratio between the exciton peak and the trion peak. Figure 2-9 shows the photoluminescence of transferred WS_2 on Si/SiO_2 substrate and sapphire substrates. The PL on the sapphire possesses a higher I_{A^-}/I_A ratio, which means that on the sapphire more electrons are injected to the WS_2, suggesting more charge transfer. Moreover, the intensity on the sapphire substrate is quenched which might be due to the non-radiative recombination via the sapphire substrate [5].

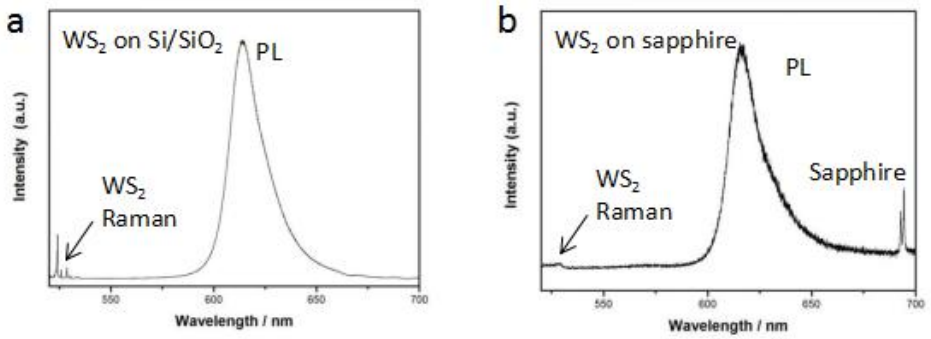

Figure 2-9. Photoluminescence of WS_2 monolayer triangles transferred on Si/SiO_2 (a) and on sapphire (b). The PL peak, Raman peaks of WS_2 monolayer, and Raman peaks of sapphire are labeled in the spectra.

2.4.4 Raman spectroscopy of TMD monolayers on different substrates

As the photoluminescence shows a different response on various substrates, the Raman spectra of TMD monolayers are also affected by the transfer process. Since there is little strain from the substrate, there will not be significant changes in either the E' modes or the A'$_1$ modes [4].

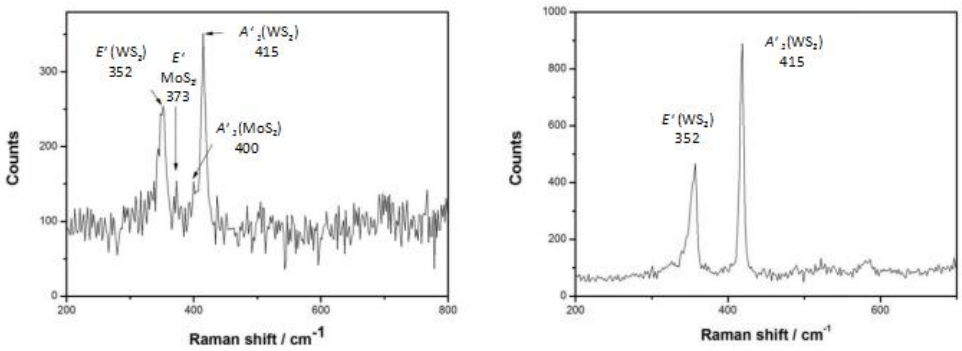

Figure 2-10. The Raman spectra of $WMoS_2$ monolayer (left) and WS_2 (right) monolayer triangles on the sapphire substrate. The Raman peaks and their positions are labeled in the spectra.

Figure 2-10 shows the Raman spectroscopy of $WMoS_2$ alloy (left) and WS2 (right) monolayer triangles on the sapphire substrate under 514.5 nm excitation laser. The 2LA acoustic

modes of WS_2 are obviously quenched on the sapphire substrate. As is discussed in the chapter 1, the generation of 2LA acoustic modes of WS_2 under resonant laser includes a transition from the valence band to the conduction band. The non-radiative recombination property of sapphire inhibits the transition process and quenches the emission of photons. Therefore, the signal of the 2LA modes is largely quenched as well as the photoluminescence signal.

2.4.5 Heterostructures of 2D materials via transfer

In our work, homostructures and heterostructures of TMD layers are synthesized via wet chemical deterministic transfer. In the deterministic transfer process, firstly the wafer with TMD layers is spin coated with polymer carrier layer (PMMA) and adhered to transparent acetate film, and then the TMD layers together with the film are released from the original substrate, which is similar to the regular wet transfer. The TMD triangle island is located under an optical microscope with the help of a small window in the acetate film and deposited at the position of interest on the target substrate with a micro-manipulator. In the end, the polymer layer is removed, leaving the TMD layer at the desired position.

Before we look into the properties of stacked layers, it is important to know how the substrate affects their properties. A stacked MoS_2 bilayer sample is shown in Figure 2-11, and because of the artificially stacking process, the bilayer structure is twisted. The optical image has a good contrast so that we can decide the twisted angle by measuring the angle between the edges of the two triangles. As is shown in the figure, the twisted angle for this sample is 30°. Then we applied a filter of 670 nm wavelength to observe the sample in the fluorescent mode and is shown in Figure 2-11 (b). We observe quite strong fluorescent signal from the sample, which is consistent with the emission energy of monolayer MoS_2 and demonstrates the crystalline quality of the MoS_2 monolayer triangles. In the stacked bilayer area, the fluorescence is obviously

brighter than the monolayer area, so that the emission is enhanced when the monolayer MoS_2 is stacked. In order to investigate on the enhancement of the signals, we conducted a line scan of photoluminescence as well as Raman intensities across the monolayer and bilayer area of the samples, starting from the point O to the point X. The labeled points (a), (b), and (c) are used to locate the edges of the heterostructure. The points (a) and (c) are on the edges of the sample, while the point (b) is the division between the monolayer area and the bilayer area. From the PL line scan in Figure 2-11 (c), we find that the PL intensity of the bilayer area is almost twice of the monolayer. The stacked bilayer MoS_2 has enhanced PL rather than quenched PL in a real bilayer MoS_2. This is due to the PMMA or liquid residue remaining between the two layers after transfer, preventing the coupling of the layers. If the sample is annealed substantially after transfer, the PL in the bilayer area gets quenched, which will be discussed in the following chapter. For the Raman line scan shown in (d), we find that the A'_1 peak intensity has about 1.8 times enhancement after stacking. The mechanism of Raman enhancement of this sample should be the same as that of photoluminescence. However, after annealing, the Raman is still enhanced instead of being quenched, although the ratio is different compared to the ratio before annealing. This will also be fully discussed in the next chapter.

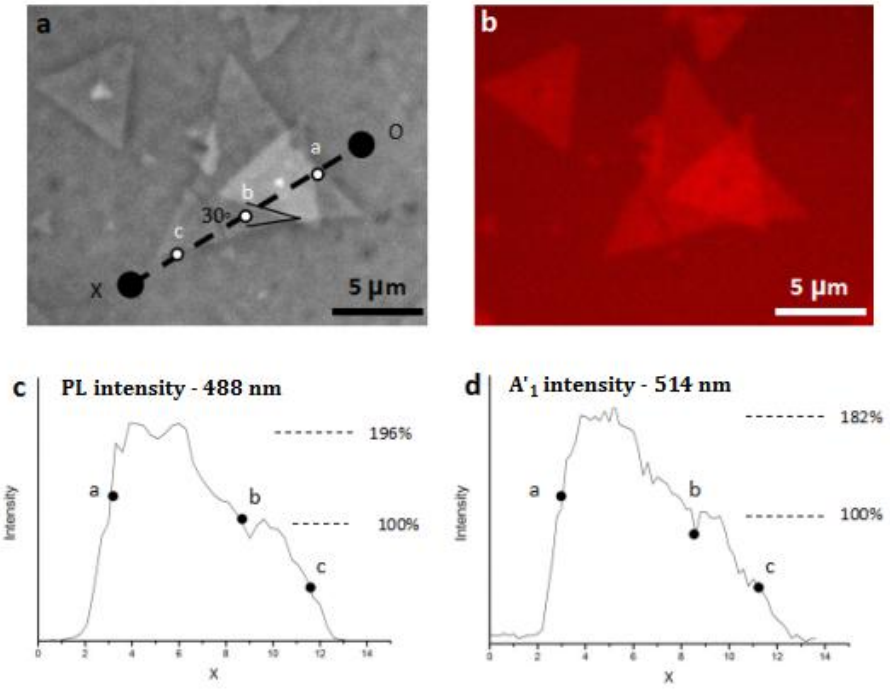

Figure 2-11 (a) Optical image (50X) of stacked bilayer MoS_2; (b) Fluorescent image (50X) of stacked bilayer MoS_2; (c) PL line scan from the point O to the point X; (d) A'_1 peak line scan from the point O to the point X.

What we will discuss in this section is the PL and Raman at the points of the edges. At point (a), the PL and Raman intensities jump abruptly from substrate background to the bilayer area. At point (c), they jump from monolayer area intensity to the background intensity. However, around point (b), there is a 'valley' in the line scans of both PL and Raman spectrum. The interruption of the curves is probably due to strain on the division between the bilayer area and monolayer. Since the stacked layers are constructed by transferring a monolayer on another monolayer when the top layer covers the edge of the bottom triangle, it is stretched by gravity and therefore strain is induced in the top layer. Moreover, the non-flat edge can also scatter photons, resulting in the loss of signal got by the counter. These may be the reasons for the interruption in the curves. The signals in the center of the bilayer and monolayer region are somehow smoother and therefore when we study the PL and Raman of the heterostructures, the regions near the

edges should be excluded, and the center area is preferred.

2.5 Conclusion

The wet transfer method is easy to perform, and it is commonly used for transferring 2D materials from SiO_2/Si or sapphire wafers onto other substrates. The problems that come with wet transfers include a high chance of contamination, and sometimes etchants damage the samples. However, we can anneal the sample at 300℃ under low pressure to recover the properties of 2D samples.

Optical images have shown that the crystalline quality of TMDC monolayer triangles after transfer is good. Raman and Photoluminescence spectra of the transferred samples are changed compared to the as grown ones, including shifts of peak positions, quenching or enhancement of intensity, and changing of the weight of trion peak. These changes result from released strain after transfer, or the doping effects of substrates, and they need to be considered when investigating the properties of heterostructures made by transfer methods.

References

1. Z. Lu, L. Sun, G. Xu, J. Zheng, Q. Zhang, J. Wang, L. Jiao. Universal Transfer and Stacking of Chemical Vapor Deposition Grown Two-Dimensional Atomic Layers with Water-Soluble Polymer Mediator, ACS Nano, 2016, 10, 5237–5242.

2. H. J. Conley, B. Wang, J. I. Ziegler, R. F. HaglundJr., S. T. Pantelides, K. I. Bolotin. Bandgap Engineering of Strained Monolayer and Bilayer MoS_2, Nano Lett., 2013, 13, 3626–3630.

3. K. F. Mak, K. He, C. Lee, G. H. Lee, J. Hone, T. F. Heinz, J. Shan. Tightly bound trions in monolayer MoS_2. Nature Materials 2013, 12, 207–211.

4. Y. Li, Z. Qi, M. Liu, et al. Photoluminescence of monolayer MoS_2 on $LaAlO_3$ and $SrTiO_3$ substrates, Nanoscale 2014, 6, 15248.

5. L. Su, Y. Yu, L. Cao, Y. Zhang, Effects of substrate type and material-substrate bonding on high-temperature behavior of monolayer WS_2, Nano Res. 2015, 8, 2686.

6. D. Ma, J. Shi, Q. Ji, Y. Zhang, M. Liu, Q. Feng, X. Song, J. Zhang, Y. Zhang, Z. Liu. A universal etching-free transfer of MoS_2 films for applications in photodetectors, Nano Res. 2015, 8, 3662.

Chapter 3

Properties of Twisted MoS_2 Bilayers

3.1 Introduction

The properties and performance of materials always rely on their structures. In 2D materials, the concept of 'structure' usually refers to the atomic coordination, the number of layers, and the stacking sequences [1,2]. These structural factors affect the electronic properties and vibrational properties of 2D materials by changing the crystal symmetry, and hence they are significant in the engineering of 2D complex systems. It is well known that the properties of TMDC are layer-dependent. As the number of layers goes from bulk to monolayer, MoS_2 and WS_2 crystals undergo a transition from the indirect band gap to the direct band gap [3]. This unique property of semiconducting TMDs makes them promising in the field of the next-generation optoelectronics. Apart from electronic properties, the symmetry of the lattice also depends on the number of the layers. In even-number-layered TMD crystals, the structure has inversion symmetry and therefore the electronic states are doubly spin-degenerate [3]. However, in odd-number-layered TMD crystals, the inversion symmetry is broken resulting in valence band splitting. In monolayer MoS_2 crystal, the band split is about 160 meV [3]. The breaking of inversion symmetry of odd-number-layered TMD can be observed by second harmonic generation (SHG).

As well as many other layered materials, there are different polytypes of MoS_2 with distinct stacking orders: these include the 2H phase (P63/mmc space group) and the 3R phase (R3m space group) which are shown in Figure 3-1 [4]. Unlike the 1T phase of MoS_2, both the 2H phase and the 3R phase have trigonal prismatic coordination [4]. In the 2H phase, the S(Mo) atoms of every layer locate upon the Mo(S) atoms of the adjacent layer [4], and S(Mo) atoms of the third layer locate exactly upon the S(Mo) position of the first layer, as is shown in Figure 3-1(a). In the

3R phase, the first layer and the third layer are different, which is shown in the Figure 3-1(b). The Mo atoms of the second layer stay below the S atoms of the top layer and upon the hollow sites of the bottom layer, while the S atoms locate upon the Mo atoms of the bottom layer and below the hollow sites of the top layer. For chemical vapor deposition (CVD) grown bilayer MoS_2 there may be different stacking orders and crystal orientation rotations. Bilayer MoS_2 could exhibit two stacking orders: two layers in the same orientation (AA stacking) and in the reverse orientation (AB stacking). The AA stacking is similar to the 3R configuration, while the AB stacking exhibits the 2H configuration. However, there are other stacking possibilities in which the layers are rotated by specific angles (see next section).

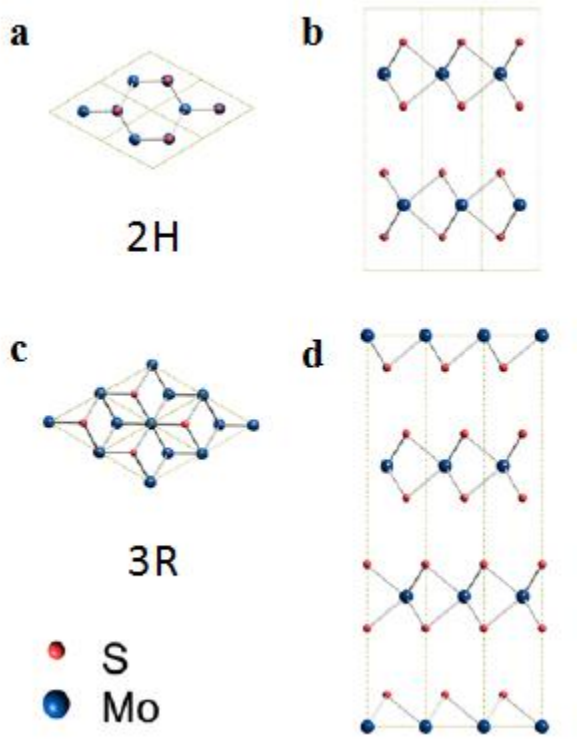

Figure 3-1 Schematic illustration of the structures of layered MoS_2[4]. (a) The top view and (b) the side view of the 2H phase MoS_2. (c)The top view and (d) the side view of the 3R phase MoS_2. The red spheres present the S atoms while the blue spheres sandwiched between red spheres present the Mo atoms [4].

3.2 Moiré pattern

Moiré patterns come from the interference of patterns at a large scale. When two identical but similar lattices are overlaid on each other with a small rotation or displacement, the moiré effect will appear in the superposition [5]. In the field of layered materials, most materials possess periodic crystalline structures so that moire patterns will appear when one layer of a 2D material is overlaid on another layer with different lattice parameters or is overlaid on the same kind of layered material with a twisted angle.

TMDs and graphene are layered materials with hexagonal lattices. Therefore moiré patterns can be found in multiple layered TMD and graphene if there is a rotation between the adjacent layers. Figure 3-2 shows the moire pattern found in multilayer graphene under STM. The left figure shows the pattern in large scale, and the right figure has a higher resolution. From the high resolution image, it is found that the moiré pattern consists of larger circular spots and smaller spots. Bright areas refer to high density electron clouds, and vice versa, the darker areas refer to the low density of the electron clouds. The pattern shows periodic features on the scale of nanometers, which is about 10 times the scale of a graphene unit cell. This large scale pattern is called superlattice.

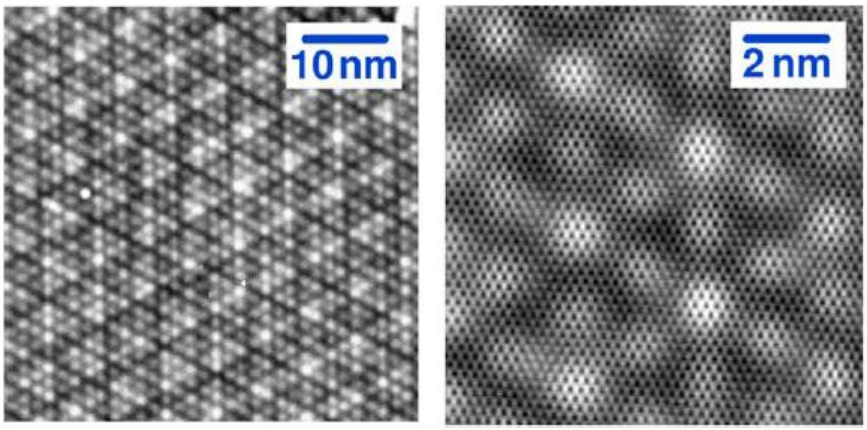

Figure 3-2 (a)The STM topograph of the moire patterns of a multilayer epitaxial graphene sample. (b) A high resolution image from (a) [6]. The bright spots form a 'super' lattice, which exhibits the moire pattern of the twisted bilayer.

To study the properties of the moiré patterns in twisted bilayer materials, the size of the superlattice unit cell is important. The unit cell parameter of the interfered pattern can be evaluated from the misaligned reciprocal vectors of the lattice [6]. Figure 3-3 is the Brillouin zone of a bilayer hexagonal lattice with a twisted angle of θ. The superlattice reciprocal vector is presented by the difference between the original reciprocal lattice vector K and the reciprocal vector of rotated lattice K_θ. $\Delta K = K - K_\theta$. The superlattice reciprocal vector gives us the equation of the size of the unit cell [5]:

$$D = 2\pi / \Delta K = 2\pi / (K - K_\theta) = a / 2 \sin(\theta/2), \quad (3\text{-}1)$$

And the orientation of the superlattice:

$$\varphi = \pi / 6 - \theta/2. \quad (3\text{-}2)$$

Here, a is the C-C bond length in graphene.

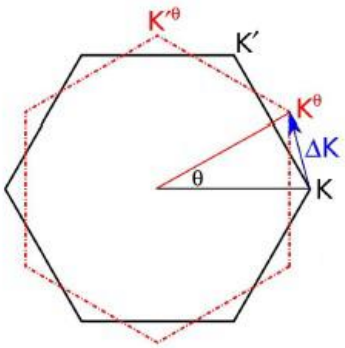

Figure 3-3 The Brillouin zone of the twisted bilayer hexagonal lattice (graphene, transition metal dichalcogenides, hBN etc.).

According to equation (3-1), when the twisting angle θ is very small, the length of the superlattice cell would be very large. As we increase θ, the cell size would become smaller. Because of the hexagonal symmetry, we can always find a pair of vectors K and K_θ with rotation less than π/6. Therefore, when θ is equal to π/6, the cell size reaches the minimum value which

should be 1.932*a* according to the equation. From the calculated cell size - angle relationship, it is expected that the electronic and optical properties of the twisted bilayer 2D materials vary with the twisted angle, and the bilayer twisted by $\pi/6$ (30°) would be interesting to study since it possesses the minimum cell superlattice size.

Apart from theoretical studies, there are also experimental results showing that the properties of twisted bilayers are dependent on the twisted angles. S. Huang *et al.* studied the band structure of twisted bilayer MoS_2[8] and demonstrated that the indirect band gap is angle-dependent, which varied from 1.20 eV at 0° to 1.51 eV at 30°. The direct band gap was slightly affected by the twisted angle and varied from 1.77 eV at 0° to 1.84 eV at 30°. K. Kim *et al.* found that in the twisted bilayer of graphene, Van Hove singularities occur in the density of states (DOS). The energy difference between conduction and valence band Van Hove singularities is angle-dependent and can reach a few eV in the case of higher twisted angles[9]. A strong resonance of the G Raman mode is observed at an intermediate angle around 10° resulting from the Van Hove singularities. At the same time, the intensity and width of the 2D Raman mode again shows angle dependence, which is attributed to the interference between Raman scattering pathways [9].

There are still novel features to be found in moiré patterned bilayer materials, in our work, the twisted bilayer of MoS_2 is studied. The results of the characterizations of this system will be shown in the following section.

3.3 The Photoluminescence of stacked MoS_2 monolayers

We have been able to stack MoS_2 triangles using the deterministic transfer method which was discussed earlier. These stacked MoS_2 triangles are decoupled and exhibit various twisting angles, the optical images of them are shown in Figure 3-4(a) and (b). The area of stacked layers and single layers can be recognized since more layers of materials scatter more incident light and

resulting in a different contrast. Figure 3-4(c) and (d) are the corresponding fluorescent images. The stacked region is brighter than the monolayer region which means the stacked layer is able to produce more fluorescence than monolayers. Comparison of the PL intensity in the stacked region and monolayer is shown in Figure 3-5 and the result is consistent with that from the fluorescent images. Stacked MoS_2 triangles are able to produce almost twice the photoluminescence of monolayer MoS_2 without changing the position of the PL main peaks. This is an important characteristic for applications in optoelectronic devices because extremely strong signal could be produced by stacking monolayer triangles.

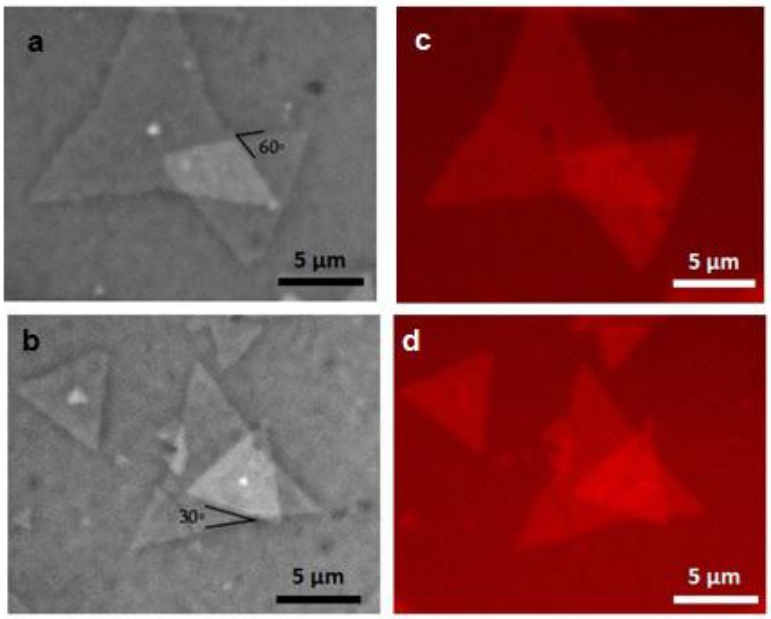

Figure 3-4. (a) and (b) Optical images of stacked MoS_2 islands. The dark lines describe the edge of the triangles, and the angle between the two lines stands for the twisted angle of the bilayer sample. (c) and (d) Fluorescent images of stacked MoS_2 islands in (a) and (b), respectively.

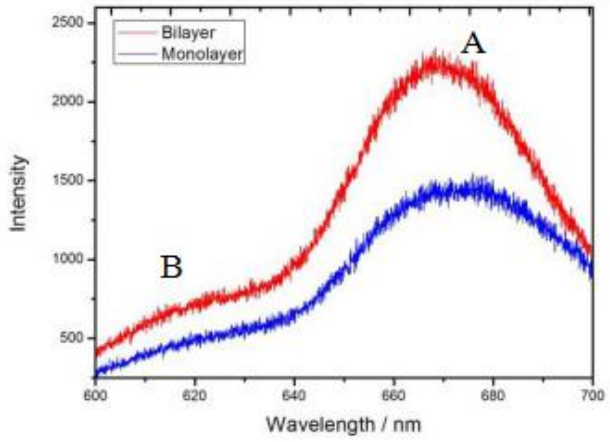

Figure 3-5 Photoluminescence of stacked MoS_2 triangles. The PL peak A and B were labeled.

In order to obtain more accurate ratios of the PL enhancement at different twisted angles we did line scans across the stacked triangles including both the bilayer and the monolayer area. The PL spectra were obtained by exciting the sample with a 488 nm laser. The power of the laser illumination at the sample was 20 μW and the line scan was obtained with a step of 0.2 micron meter. The optical images and PL line scans of two stacked MoS_2 with different twisted angles are shown in Figure 3-6. The signals fluctuate when the scan point goes through the edges, but in the center of the bilayer as well as the monolayer area, we can find relatively stable regions, and the average PL value is that of the bilayer/monolayer area. Figure 3-6 (c) is the PL line scan of a 60° twisted bilayer MoS_2, while (d) shows the PL line scan of a bilayer MoS_2 twisted by 30°. The ratio I_{2L} / I_{1L} is 1.89 and 1.96 for these two bilayers, respectively. There is a very small difference between the ratios. In order to find the influence of the twisted angles on the photoluminescence, more twisted bilayer samples were studied. The intensity ratios for bilayers with some other twisted angles are listed in Tale 3-1.

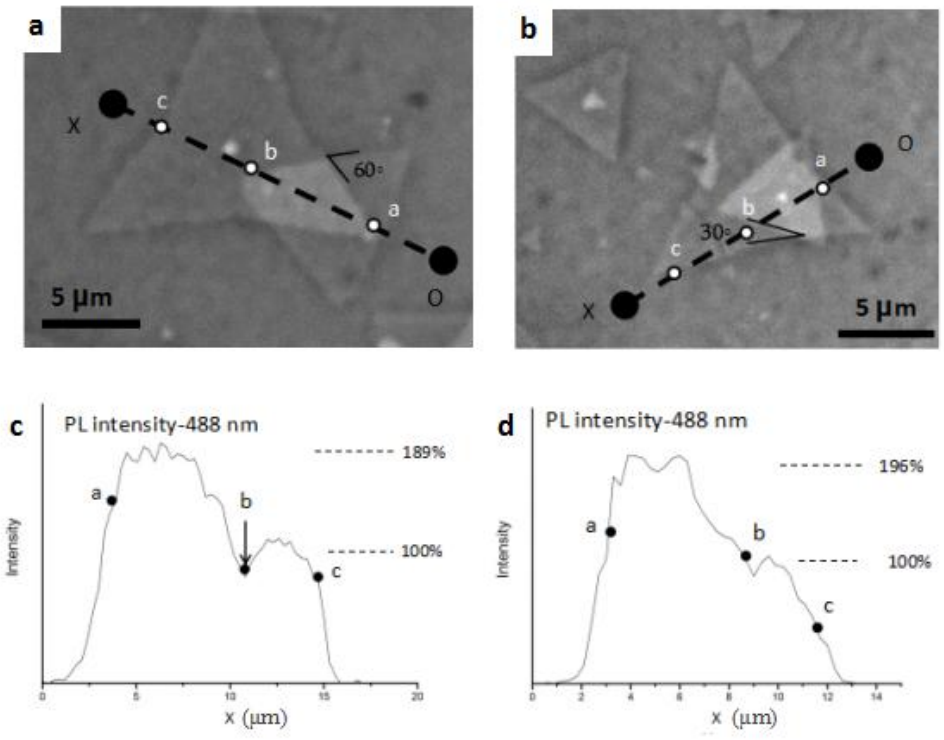

Figure 3-6 Optical images of the twisted bilayer MoS_2: (a) θ = 60°; (b) θ =30°. (c) and (d) are the line scans of the photoluminescence spectra across the bilayers in (a) and (b), respectively. Point O is the starting point and X is the ending point of the scan. Point *a*, *b* and *c* are labeled to show the edges of the monolayer and bilayer area.

Table 3-1. The intensity ratio of I_2L / $I_1L$for stacked bilayer MoS_2 with different twisted angles.

Θ(°)	0	5	17	30	42	60
I_{2L} / I_{1L}	1.89	1.82	1.80	1.96	1.78	1.90

After collecting the data of PL intensity ratios from different twisted bilayers, we find that the ratios of I_{2L} / I_{1L} stay between 1.80 - 1.90 for most of the samples, and there is no strong dependence on the twisted angles. Because the twisted bilayers that we prepared by deterministic transfer are not coupled, there are very weak interactions between the two layers so that the twisted angles will not affect the PL intensities. If annealing treatment is conducted after the

transfer, the layers will be coupled and the photoluminescence will be quenched similar to the Bernal-stacked bilayer MoS_2. At the same time, the twisted angles starts to have an impact on the photoluminescence, by changing the position and weight of the trions peaks and neutral exciton peaks and the bound exciton peaks [8].

3.4 The Raman spectra of stacked MoS_2 structures

Raman spectroscopy of the stacked region was measured and compared to Raman signals of the monolayer region, as is shown in the Figure 3-7. Similar to the PL performance, the stacked layer exhibits higher intensity in Raman modes for both E' and A'_1. The intensity enhancement is characterized by the intensity ratio $I_{A'1}(2L)/I_{A'1}(1L)$. Unlike the PL intensity ratio, the ratio of the Raman intensity is far less than 2.0, which means that considerable amount of Raman intensity is lost in the twisted bilayer system. The intensity ratios vary from 1.1-1.4 when using an excitation laser of 514.5 nm. When we further measured the intensity ratios for stacked layers with different twisting angles, it was found that the intensity ratio depends on the twisting angle. The experimental relationship is shown in Figure 3-8: for stacked triangles with a very little twisting angle (almost 0°), the intensity ratio is around 1.1 and increases gradually when the twisting angle is increased. At 30°, the intensity ratio reaches the largest value around 1.4; After 30°, it starts going down until reaching a twisting angle of 60° which is the sample state at 0°according to the hexagonal structural symmetry of TMD materials.

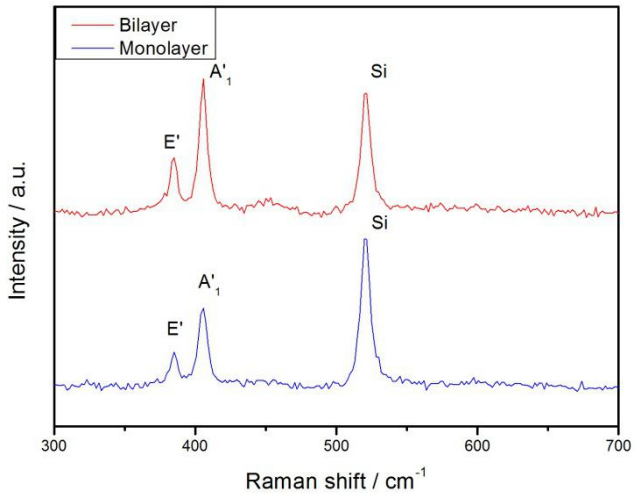

Figure 3-7. Raman spectra of stacked MoS_2 triangles. The red curve represents the Raman spectra obtained from the stacked bilayer area, while the blue curve represents the Raman spectra obtained from the monolayer area.

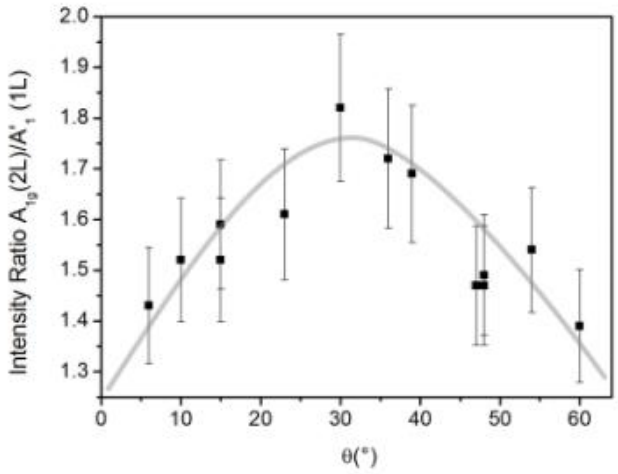

Figure3-8. The relationship between intensity ratios and the twisted angles of stacked MoS_2 layers. The curve aims to show the dependence on the twisted angles. Error bars are labeled. Calculation of the error bars are shown in Appendix B.

Raman spectra of the stacked islands were also obtained under excitation of 488 nm (blue). It can be seen from Figure 3-9 (a) that a similar relationship between intensity ratio and

the twisting angle is observed at 488 nm, but the intensity is lower compared to those obtained at 514 nm.

The twisted bilayer MoS_2 samples were annealed (forming gas, 400℃, 3h) for interlayer coupling. The Raman spectra taken under excitation of 514 nm and 488 nm laser are shown in Figure 3-9 (b). Raman intensities of A_{1g} modes in the twisted MoS_2 bilayers are still angle-dependent and reach the maximum value at θ=30°. Intensities of A_{1g} modes are enhanced after annealing, I_{A1g} can be more than 2 times that of the $I_{A'1}$in monolayer.

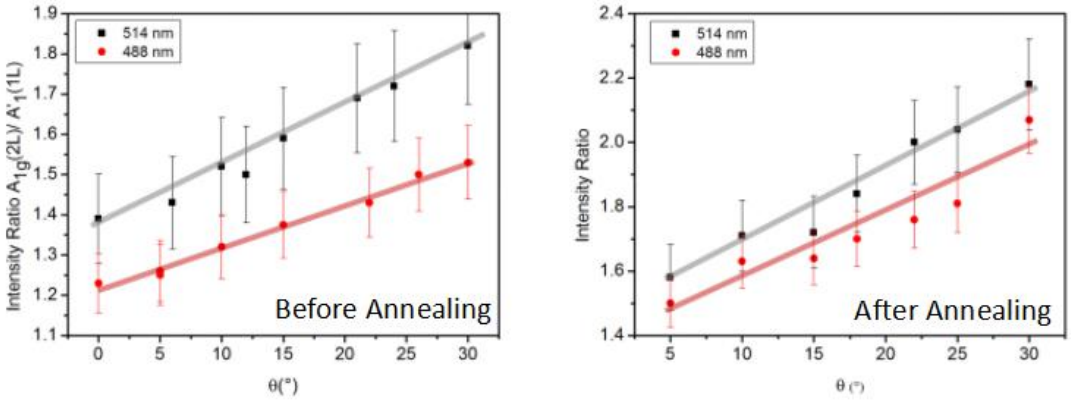

Figure3-9. Normalized A_{1g} Raman intensity of twisted bilayer MoS_2 before annealing (a) and after annealing (b) at different excitation laser lines. Error bars are labeled. Calculation of the error bars are shown in Appendix B.

3.5 Discussion

In the electronic band structure of monolayer MoS_2, the extrema of the conduction band and the valence band locate at the *K* point, and thus the monolayer MoS_2 has a direct band gap [3]. The orbital compositions of the states are shown in Figure 3-10. It is found that the critical points at the conduction band (K_C, Q_C) and the one at the valence band (K_V, Γ_V) are composed of

different orbitals. The majority of them are the d orbitals (d_{z2}, d_{xy}, d_{x2-y2}) from the Mo atoms, which are screened by the layers of S atoms. Point K_C and K_V also contain the p_x, p_y orbitals of S atoms, which are not significantly affected by the interlayer forces since their in-plane orientations. However, point Q_C and Γ_V contain the p_z orbitals of S atoms, which can have direct interaction with the adjacent layers. Therefore Q_C and Γ_V are sensitive to inter-layer interactions, and this is the reason for the layer-number-dependent properties of TMDs[3]: In monolayer MoS_2, the energy gap between Q_C and Γ_V is larger than the direct band gap, but in multilayer MoS_2, Q_C - Γ_V gap is reduced due to the interlayer interaction and is smaller than the direct band gap.

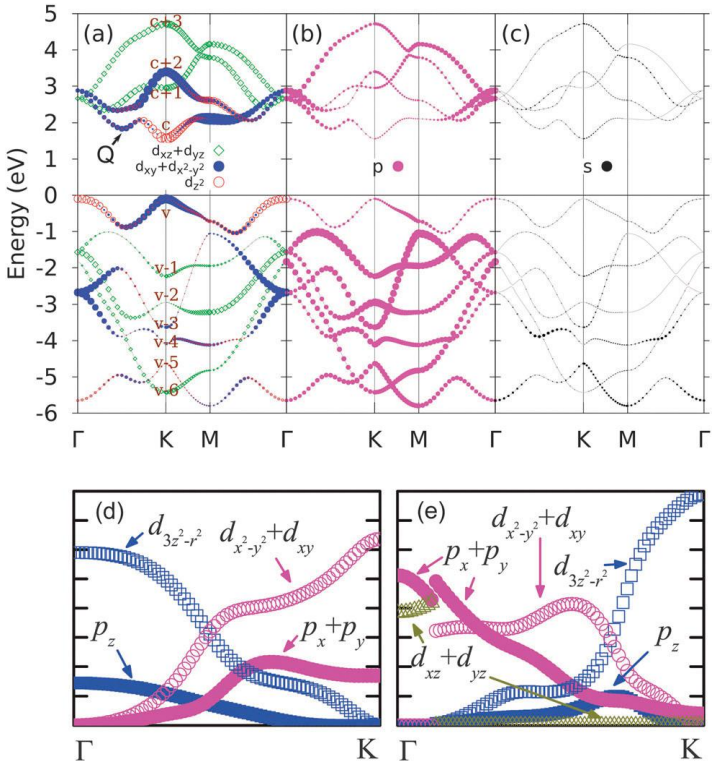

Figure 3-10. Orbital projected band structures in MoS_2 monolayer [10], and different orbitals are labeled by symbols in different colors, respectively, and symbol size is proportional to the state population. (a) d orbitals; (b) p orbitals; (c) s orbitals; (d) - (e) Orbital projected band structures of monolayer WSe_2 along the line Γ-K. (d) top valence band; (e) bottom conduction band [10].

In the case of twisted bilayer MoS_2, the interlayer interaction depends on the twisted angle. The twisted lattice reduces the interlayer coupling of the bilayer, and enlarges the Q_C -Γ_V

gap. Enlarging of the energy gap of the twisted bilayer MoS_2 has been demonstrated theoretically bu S. Huang *et al.* [8]. According to the results of the energy gaps, a possible explanation for the change of the Raman intensity ratio is the enlarged energy gap. A larger energy gap is closer to the excitation laser energy (2.54 eV for 488 nm laser and 2.41 eV for 514 nm laser) , and the system is closer to the resonant condition, and thus the Raman intensities are enhanced.

3.6 Conclusion

We have been able to stack MoS_2 triangles using the wet chemical transfer method which was discussed in the last chapter. These stacked MoS_2 triangles were decoupled, and exhibited various twisting angles. Enhancement of Photoluminescence and Raman peaks were observed in the stacked triangles. Stacked MoS_2 triangles were able to produce twice the photoluminescence emission of monolayer MoS_2. The Raman signal enhancement was characterized by the intensity ratio $A_{1g}(2L)/ A'_1(1L)$, and the intensity ratio was found to be related to the twisted angle of the stacked structure. At the twisting angle of 30 degree, the enhancement was the strongest. The intensity ratios also varied under different excitation lasers. According to the calculation results of the energy gaps, a possible explanation for the change of the Raman intensity ratio is that the energy gap was enlarged when the stacked MoS_2 bilayer was twisted 30 degree, and resulting in the change of Raman peak intensities.

References

1. Y. Lee, D. Tran, K. Myhro, J. Velasco, N. Gillgren, et al. Competition between spontaneous symmetry breaking and single-particle gaps in trilayer graphene, Nat. Commun. 2014, 5, 5656.

2. C. H.Lui, Z. Li, K. F. Mak, E.Cappelluti, T. F. Heinz, Observation of an electrically tunable band gap in trilayer graphene, Nat. Phys. 2011, 7 (12), 944−947.

3. K. F. Mak, C. Lee, J.Hone, J. Shan, T. F. Heinz, Atomically Thin MoS_2: A New Direct-Gap Semiconductor, Phys. Rev. Lett. 2010, 105, 136805.

4. J. Yan et al. Stacking-Dependent Interlayer Coupling in Trilayer MoS_2 with Broken Inversion Symmetry, Nano Lett. 2015, 15, 8155−8161.

5. I. Amidror, Moire patterns between aperiodic layers: quantitative analysis and synthesis, JOSA A 2003, 20, 1900-1919.

6. D. L. Miller et al. Structural analysis of multilayer graphene via atomic moiré interferometry. Phys. Rev. B 2010, 81, 125427

7. C.J. Tabert and E.J. Nicol. Optical conductivity of twisted bilayer graphene. Phys. Rev. B 2013, 87, 121402.

8. S. Huang, et al. Probing the Interlayer Coupling of Twisted Bilayer MoS_2 Using Photoluminescence Spectroscopy, Nano Lett. 2014, 14, 5500−5508.

9. K. Kim, S. Coh, L. Z. Tan, W. Regan, et al, Raman Spectroscopy Study of Rotated Double-Layer Graphene: Misorientation-Angle Dependence of Electronic Structure, PRL 2012, 108, 246103.

10. G. Liu et al. Chem. Soc. Rev., 2015, 44, 2643--2663.

Chapter 4

Properties of Twisted WS_2/MoS_2 Heterostructures

4.1 Introduction to TMD - TMD stacked bilayers

As is mentioned in the first chapter, heterostructures of two dimensional materials are realiezed by assembling one-atomic-thin blocks with various layered materials in a desired chosen sequence and structure. The layer-by-layer stacked structures are covalently bonded in-plane, and relatively weakly bonded by van der Waals forces between layers. Apart from the graphene - hBN stack and the graphene - TMD stack, the TMD -TMD stack is also receiving a lot of attention in the experimental field as well as the theoretical field.

The TMD - TMD stacked heterostructures can have novel properties when compared to the pristine TMD material. It has been demonstrated theoretically that the electronic band structures and optical properties of TMD - TMD stacks are tuned according to different stacking orders. For example, WS_2/MoS_2 heterobilayers have an indirect band gap, while the WSe_2/MoS_2 heterobilayers have a direct band gap [1], which could not be found in pristine TMD bilayers. The direct band gaps of the heterobilayers can be tuned from 0.79 eV to 1.16 eV with different materials and different stacking orders [1]. Moreover, it has been shown that the moiré pattern in the heterobilayer also has an impact on the properties of the heterostructure [2]. In the TMD -TMD stack system, Engineering of the band gaps can be achieved with most of the TMD features remaining, providing the TMD layered materials more possibilities for applications in novel electronic devices.

The TMD - TMD stacked bilayers can be synthesized via transfer methods or vapor-phase growth methods [3]. The heterobilayers grown by the vapor phase growth are usually well

coupled, however, the heterobilayers grown by transfer methods may not be coupled due to the polymer residues remained between the layers [4]. It has been demonstrated experimentally that the interlayer coupling can be tuned by annealing so as to obtain a well coupled heterostrucuture [4]. After annealing for 12 hours, the properties of the heterostructure shows only the indirect band gap peak and the hetero peak, thus showing good coupling between the layers [4].

In TMD - TMD stacked bilayers, there is not the only mismatch between the lattice, but also a mismatch between the band structures. Most of the TMD stacked heterostructures will form type II heterojunction, with the electrons and holes separated into different layers, which we have discussed in the first chapter.

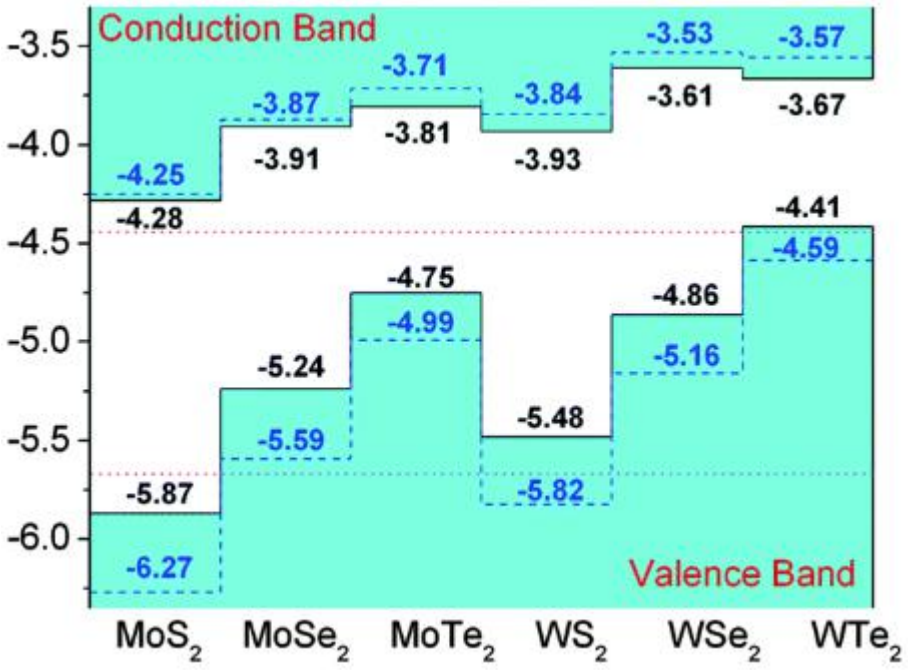

Figure 4-1. Band structures of several transition metal dichalcogenides [5]. The valence band maximum (VBM) and the conduction band minimum (CBM) are marked. The solid lines are calculated by PBE, and the dashed lines are calculated by HSE06 [5].

For example, according to the work function diagram of the TMD monolayers listed in Figure 4-1, when a heterojunction of WS_2/MoS_2 is formed, the MoS_2 has the lower conduction band minimum, and the WS_2 has the higher valence band maximum. Therefore the electrons will

be accumulated in the MoS_2 layer, while the holes will be accumulated in the WS_2 layer.

4.2 Moiré pattern in TMD - TMD heterobilayer

Compared to the TMD twisted bilayer composed of the same material, i.e. Twisted MoS_2 bilayers, the TMD - TMD heterobilayers may have more complicated lattice mismatch. The TMD - TMD heterobilayers are made by stacking one layer of TMD onto a different TMD layer. A large number of TMD heterostructures can be constructed due to the variety of the TMD materials for example, WS_2/MoS_2, WSe_2/MoS_2, and $MoSe_2/MoS_2$. In these bilayer heterostructures, moiré patterns are formed not only due to the rotation of the lattice but also due to the lattice parameter mismatch. The lattice parameter mismatch can be quite large since there is only weak van der Waals bonding between the layers. The variability of the moiré patterns in the heterobilayer raised a question: how does the moire patterns affect the electronic structure and the optical properties of the heterostructure?

Jun Kang *et al.* performed theoretical calculations of the moire pattern in the $MoS_2/MoSe_2$ heterobilayer, and the result shows that the conduction band maximum is weakly localized, however, the valence band minimum is strongly localized [6]. These authors divided a moiré pattern super cell into six parts: I^A - VI^A for the $MoSe_2$ layer, and I^B - VI^B for the MoS_2 layer. The distribution of the CBM and VBM are shown in Figure 4-2. The CBM states are weakly localized in the MoS_2 layer, and the VBM are localized around III^A and the IV^A area in both layers. The localization of the states is probably due to different inter-layer coupling at different parts of the pattern [6]. Since charge separation occurs in most of the TMD - TMD heterobilayers, the localized states may be a general feature for the TMD - TMD bilayer stacks and may affect the properties of the heterostructures. In our work, we will study the properties of twisted WS_2/MoS_2 heterobilayer, and find experimental evidence of the states localization.

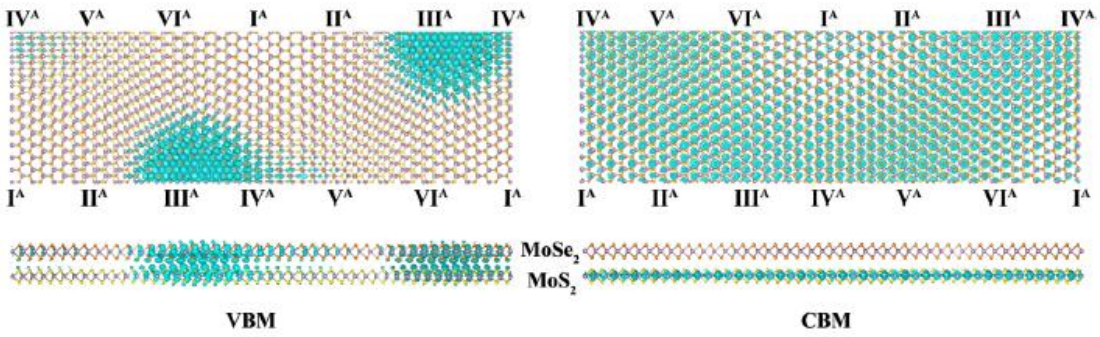

Figure 4-2. Distribution of the VBM states (left) and the CBM states (right) for twisted $MoS_2/MoSe_2$ heterostructures [6]. The VBM states are found to be strongly localized.

4.3 Twisted WS_2/MoS_2 bilayer heterostructures

The fabrication of WS_2/MoS_2 twisted hetero-bilayers was realized by stacking triangular WS_2 monolayers on top of MoS_2 monolayer triangles.

4.3.1 TMDC single-layer triangle growth.

Monolayer triangular MoS_2 crystals were grown on 300 nm SiO_2/Si wafers via Chemical Vapor Deposition. 1 cm * 1 cm wafers were placed into a ceramic boat with 10 mg of MoS_2(≥ 99.5%, Sigma-Aldrich) on them. A ceramic boat with 300 mg of sulphur (≥99%, Sigma-Aldrich) was placed upstream. The boats were loaded into a 1 - inch quartz tube. The growth was conducted at atmospheric pressure and 700 ℃ under ultrahigh-purity argon flow (around 80 s.c.c.m). The triangular crystals form after 30 minutes of growth. WS_2 monolayers were also grown by CVD with similar conditions. We used 10 mg WO_3(≥99.5%, Sigma-Aldrich) powders instead of MoS_2, and the growth temperature was 800 ℃.

4.3.2 Heterostructure synthesis

The heterostructure was made by transferring monolayer WS_2 onto MoS_2 grown on a SiO_2/Si wafer. The WS_2 monolayer on SiO_2/Si was spin-coated with poly(methyl methacrylate) (PMMA) (495 A6) at 3,000 r.p.m. for 60 s and cured at room temperature for 8 hrs. The PMMA and WS_2 film was released from the substrate (SiO_2/Si) by NaOH etching (1 mol/L) at 80℃ for a few minutes. The film was transferred to deionized water to rinse the NaOH residue off the sample. It was then transferred onto CVD-grown MoS_2 and placed on a hot plate to dry away water. After then, acetone was used to dissolve the PMMA. Finally, the stacked bilayer heterostructures were annealed at 300℃ under forming gas with low pressure (10 torrs). The annealing process aims to improve the contact between the WS_2 and MoS_2 monolayers so that the heterostructure can be coupled firmly.

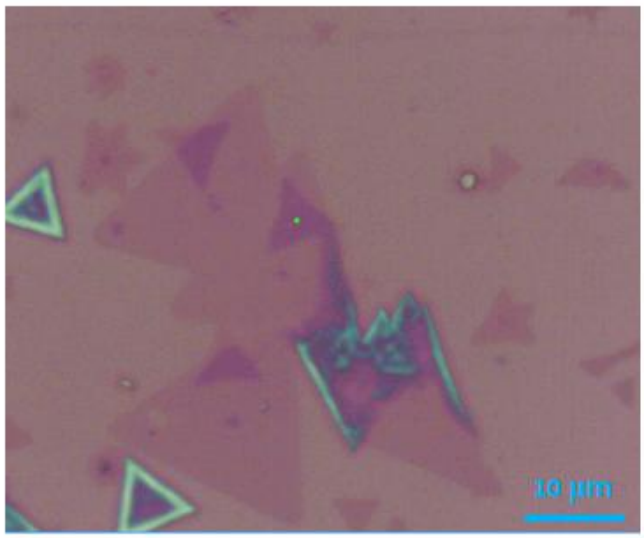

Figure 4-3. Optical images (50X) of the stacked WS_2/MoS_2 heterostructures. The larger triangles are the WS_2 (the top layer), the smaller triangles are the MoS_2 (the bottom layer), and the dark purple areas are the stacked area.

Figure 4-3 shows an optical microscope image of WS_2/MoS_2 twisted bilayers on a Si substrate coated with 300-nm SiO_2. The Mo edges of the bottom triangles and the W edges of the top

triangles can be determined from the optical images and thus the twisted angles of the bilayers are calculated by measuring the twisted angle between the Mo edge lines and W edge lines. AFM data of the twisted bilayer is shown in Figure 4-4. The thickness of the MoS_2 layer is 0.8 nm, confirming that the triangle of MoS_2 is a monolayer. The interlayer thickness is 1.0 nm, showing that the monolayer WS_2 and themonolayer MoS_2 is well coupled since 1.0 nm is a typical thickness of monolayer WS_2.

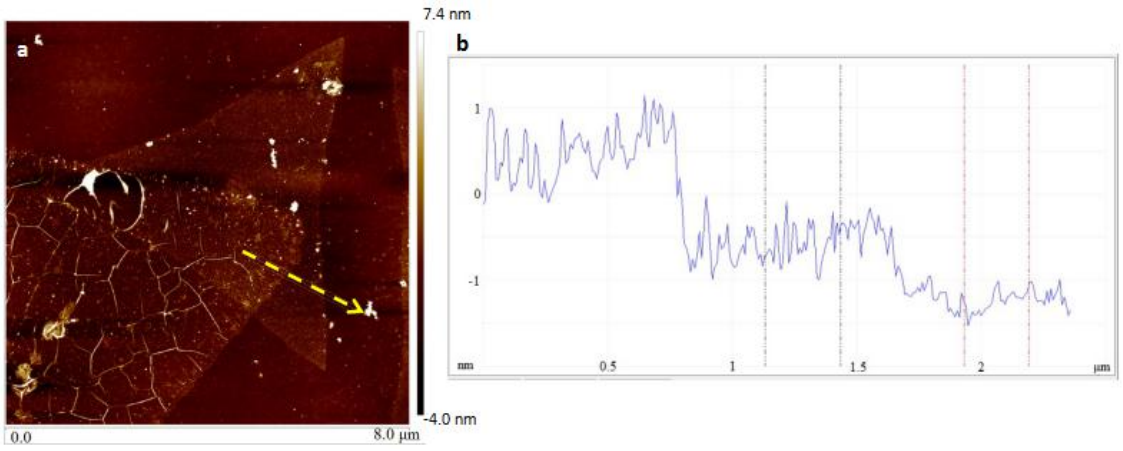

Figure 4-4. (a) Surface morphology of the stacked WS_2/MoS_2 triangels measured by AFM. (b) Height spectrum of the line scan which is labeled with a yellow dashed arrow in (a), indicating 1.0 nm interlayer distance between WS_2 layer and MoS_2 layer.

4.4 Raman spectra of the twisted WS_2/MoS_2 heterobilayer

Raman spectroscopy was used to shed light on the vibrational properties of the WS_2/MoS_2 heterostructures. Raman spectroscopy of a WS_2/MoS_2 heterostructure (untwisted) before coupling and after coupling are shown in Figure 4-5. The main Raman modes of both monolayer WS_2 and monolayer MoS_2 can be found in the spectra. When looking at the Raman above 100 cm^{-1}, the spectrum of the heterostructure is a combination of two individual layers, the peaks can be recognized as the in-plane (i.e., E') and out-of-plane (i.e., A'_1) modes of WS_2 and

MoS_2 and the acoustic modes, respectively.

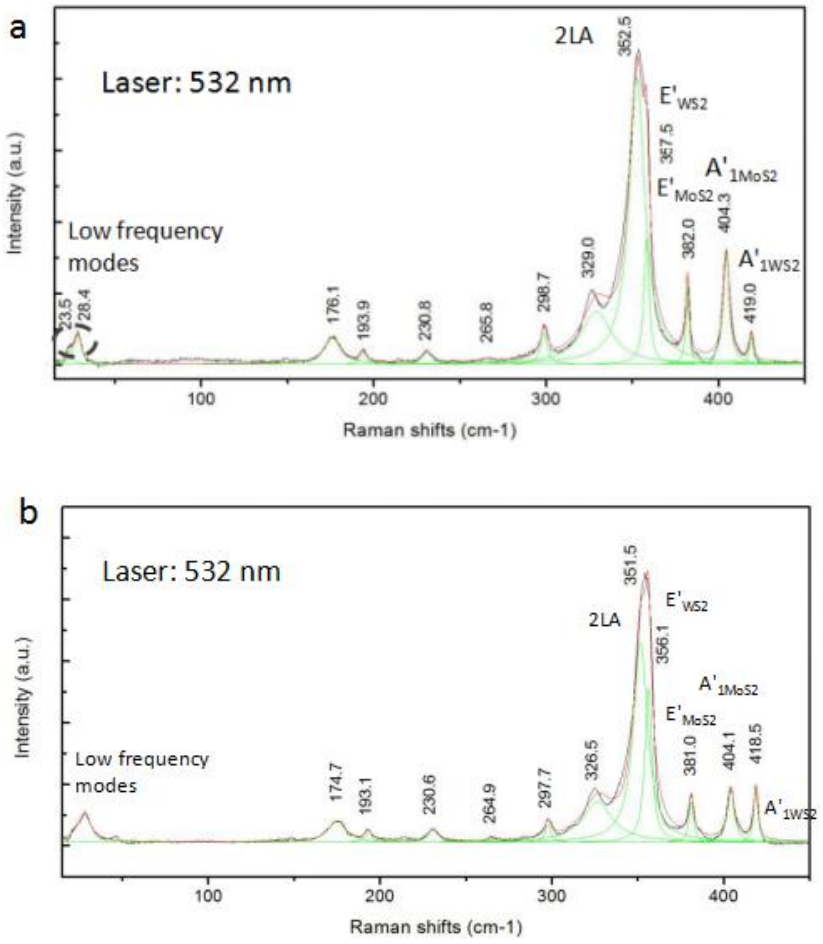

Figure 4-5. Raman spectra of stacked WS_2/MoS_2 triangles before (a) and after (b) annealing. The positions of the peaks are labeled, including 2LA, E' and A'_1 and other peaks. Errors calculations can be found in Appendix B.

Unlike the bilayer pristine WS_2, the 2LA mode around 352 cm^{-1} is still strong after the heterostructure is coupled, which means that the WS_2 keeps its monolayer properties. At the same time, for most of the Raman modes, there are shifts of less than 0.5 cm^{-1} between the heterostructures before and after coupling, and those small shifts can be explained by errors (data statistics is shown in Appendix B). However, there is a clear ~1 cm^{-1} shift in the E' peak, and

both the MoS_2 and WS_2 E' peaks are red shifted after annealing. Since the E' modes are sensitive to in-plane strain [11], it is possible that in-plane strain is induced in the procedure of annealing, resulting in the red shifts of the E' modes. In addition, we also investigated the first and second order Raman modes of an untwisted heterostructure and a heterostructure twisted by 30°, which are plotted in Figure 4-6. The dashed lines highlight the shifts of the main Raman modes of the heterostructure, and we can find from the figure that there are no significant shifts for the peaks. This result is consistent with what is shown in Figure 4-5: the interlayer coupling and the rotation of the bilayer lattice have little impact on the main Raman modes of the WS_2/MoS_2 heterostructure.

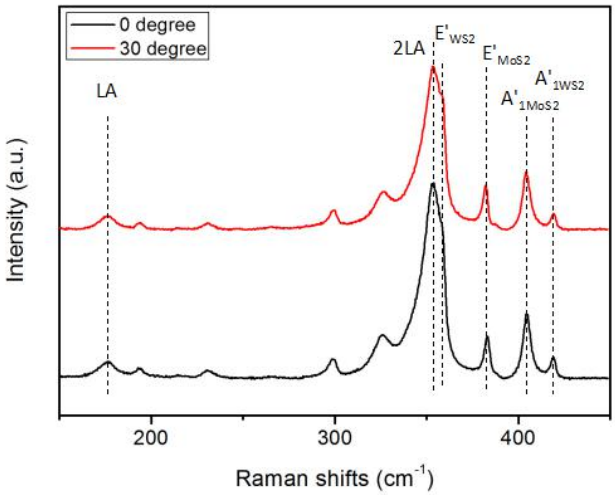

Figure 4-6. Raman spectra of stacked WS_2/MoS_2 triangles with a twisted angle of 0° and 30°. The dashed lines indicate the positions of the 2LA, E' and A'_1 peaks.

The van der Waals force is the dominant force between layered heterostructures and it is much weaker compared to the intralayer covalent forces. Therefore, their Raman features have very low frequencies due to the ultra-low bonding energy. As is mentioned in the first chapter, the Raman modes related to the van der Waals forces are usually lower than 50 cm^{-1} and are named

layer breathing modes (out of plane) and shear modes (in plane) in the Raman spectra. Thus we focus on the very low frequency modes (< 50 cm^{-1}) of stacked twisted layers by ultra-low frequency Raman.

Compared with monolayer WS_2 and MoS_2, Raman spectra of WS_2/MoS_2 stacked bilayers exhibit layer breathing modes in ultra-low frequency (0-50 cm^{-1}), which shed light on vibrational properties caused by van der Waals forces between layers. After transfer, the layers were not well coupled and the interlayer interaction should be weak. However, we still found peaks around 23 cm^{-1} and 28 cm^{-1} in Figure 4-5 indicating that there were interactions between the WS_2 and the MoS_2 layer. Annealing should help coupling the bilayer heterostructures. However, for the heterostructure after annealing, the two peaks did not show significant shifts, with one peak located at 22.3 cm^{-1} and the other at 27.5 cm^{-1}, for both the untwisted and the twisted heterostructures. The peak around 22.3 cm^{-1} possibly represents the in-plane shear mode, while the peak around 27 - 28 cm^{-1} represents the out-of-plane LBM mode. The broad peak around 45 cm^{-1}, which is not found in the decoupled samples, appeared after thermal annealing. The new peak was slightly blue shifted by 1 cm^{-1} when twisted.

The results of the low-frequency Raman modes indicate that the heterostructure is already coupled before the thermal annealing: the intensity and the position of the peaks do not change dramatically which means the inter-layer van der Waals forces are formed before the annealing and the contact between the WS_2 and the MoS_2 layers is good. During the fabrication process we transferred the WS_2 layer onto the as-grown MoS_2 layer. Because there is no PMMA residue on top of the MoS_2 the two layers could be in good contact with each other. The annealing process made a difference to the low-frequency Raman in that a new peak around 45 cm^{-1} appears. A possible explanation is that during the heating, the wrinkles on the WS_2 layer are coupled, and therefore the peak refers to the LBM mode of bilayer WS_2. In addition, a twisted lattice doesn't have impacts on the low-frequency Raman modes. Though it may affect the interaction between

layers and then affect the in-plane and the out-of-plane modes, it is less than the range of error and could not be observed. For the study of the effect of the twisted lattice, the measurement of the Photoluminescence is needed.

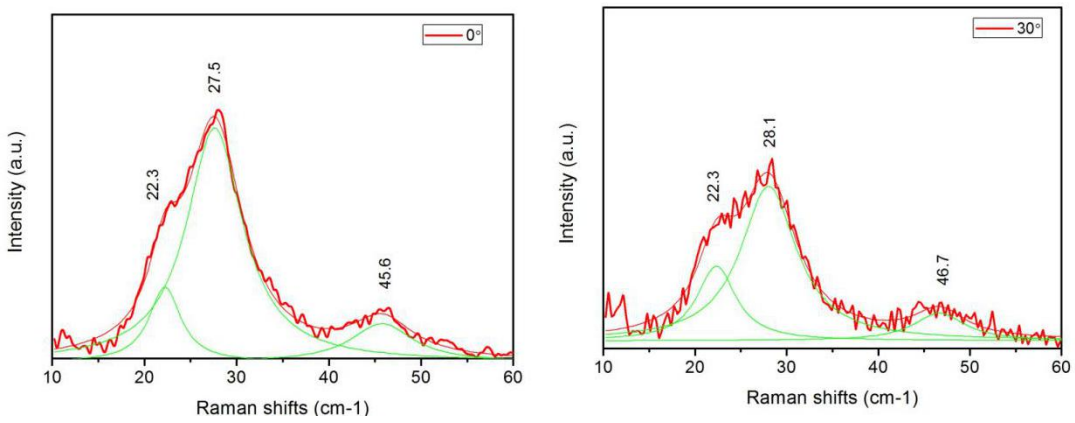

Figure 4-7. Low frequency Raman spectra of stacked WS_2/MoS_2 bilayers with twisted angles: (a) 0°; (b) 30°. The spectra are fitted with 3 Lorentz peaks, the one at 22 cm^{-1} refers to SM modes, the one at around 28 cm^{-1} refers to LBM modes, and the one at around 46 cm^{-1} refers to the wrinkles of WS_2 layer. Errors calculations can be found in Appendix B.

4.5 Photoluminescence studies of the WS_2/MoS_2 heterobilayers

To probe the optoelectronic properties of WS_2/MoS_2 bilayers, photoluminescence of the stacked heterostructures was measured. The photoluminescence changes significantly in different twisted WS_2/MoS_2 bilayers, which is shown in Figure 4-8. The PL spectra are composed of multi-peaks: MoS_2 PL peaks, WS_2 PL peaks, and also a Hetero peak which indicate interlayer coupling of the two layers. Looking at the PL of WS_2/MoS_2 twisted bilayers, the peaks of WS_2 photoluminescence is much higher when twisted by 30 degrees than untwisted bilayers and slightly twisted bilayers (around 0°). Vice versa, when twisted by 85° (around 90°), the intensity of MoS_2 photoluminescence looks slightly higher. Contrary to the quenching of photoluminescence, twisting the heterojunction partially 'releases' the quenched signals. As the

quenching is attributed to the charge transfer effect between WS_2 and MoS_2 layer, the PL seems to be related to the change of the charge transfer. This result is in accordance with expectations since twisting the heterojunction will lead to more mismatch in the lattice and have an influence on the charge transfer. Therefore, the characterizations and analysis we did in the next step aimed to find how they are affected.

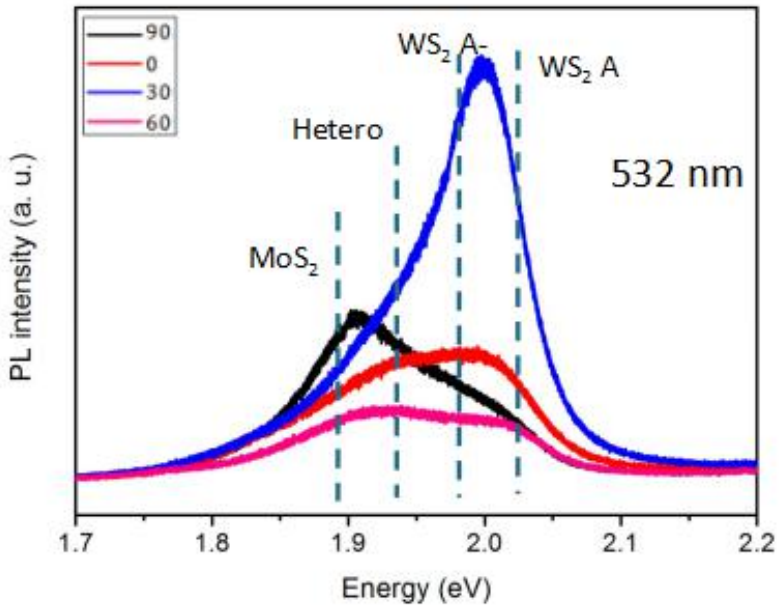

Figure 4-8. Photoluminescence of stacked WS_2/MoS_2 heterobilayers with different twisted angles. The spectra were taken under 532 nm excitation laser. The dashed lines indicate the positions of the most important emission peaks in the heterostructures.

The charge transfer process and the formation process of the 'Hetero' peak are shown in the Figure 4-9 [9]. In the heterojunction of WS_2 and MoS_2, both the valence band maximum and the conduction band minimum of MoS_2 are lower than those of WS_2. Consequently, the WS_2/MoS_2 heterostructure forms a type II heterojunction in which the conduction band minimum and the valence band maximum reside in separate materials. The charge transfer process occurs between the two materials, giving extra electrons to the conducting band (CB) of MoS_2, and extra holes to the valence band (VB) of WS_2. Therefore, in the heterojunction WS_2 is p-type doped while MoS_2

is n-type doped. Different types of doping have been observed to tune the PL of MoS_2 and WS_2 via experimental results [7,8]. Quenching of the photoluminescence is observed in a reported result of chemically n-doped MoS_2 [8] because the extra electrons will suppress the recombination of the electron-hole pairs [8].

Contrarily to the extraction of electrons in MoS_2, there is an injection of electrons in WS_2. The increase of trions in WS_2 contributes to the switch of emission mode from exiciton to trion. The p-doping would not suppress the photoluminescence, thus the intensities of the WS_2 peaks should look higher in the heterstructure. In addition, there is an energy transfer from the CBM of the MoS_2 to the VBM of the WS_2. As is shown in Figure 4-9, the energy transfer is approximately 1.94 eV, therefore the peaks we found around 1.93 eV in PL are probably the 'Hetero' peak which comes from this energy transfer. The energy and intensity of this peak vary at different orientations, later we will also discuss them.

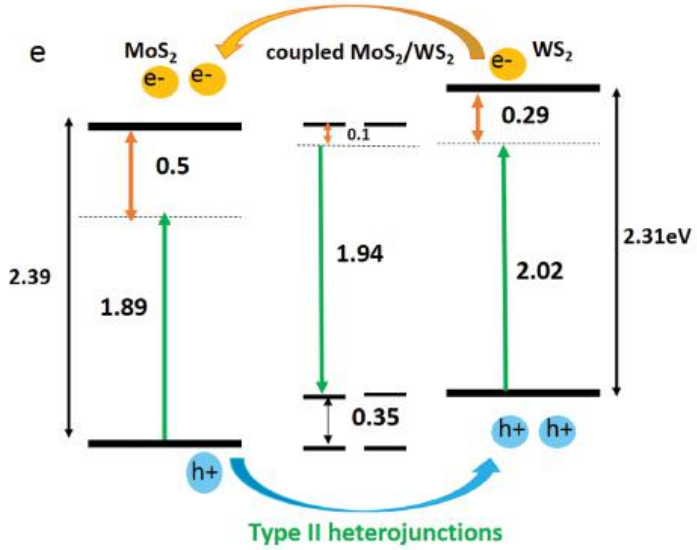

Figure 4-9. A brief illustration of the charge transfer process in the untwisted WS_2/MoS_2 heterostructures, and the formation of the Hetero peak [9].

In order to investigate the fundamentals in the change of PL, we fitted the PL curves to

show the trion (A^-) and exciton (A) of WS_2 and MoS_2 in Figure 4-10. the PL of the WS_2/MoS_2 heterostructure is mostly composed of 6 peaks: the trion (A^-) of MoS_2, exciton (A) of MoS_2, exciton (B) of MoS_2, the trion (A^-) of WS_2, exciton (A) of WS_2, and the Hetero peak. The fitting process is constrained by 3 conditions. The first constraint is that difference between MoS_2 A- and A peak is 18-50 meV [12]; The second constraint is that difference between WS_2 A- and A peak is 40-45 meV [13]; The separation between exciton (A) and exciton (B) is 0.12 - 0.15 eV [10,12].

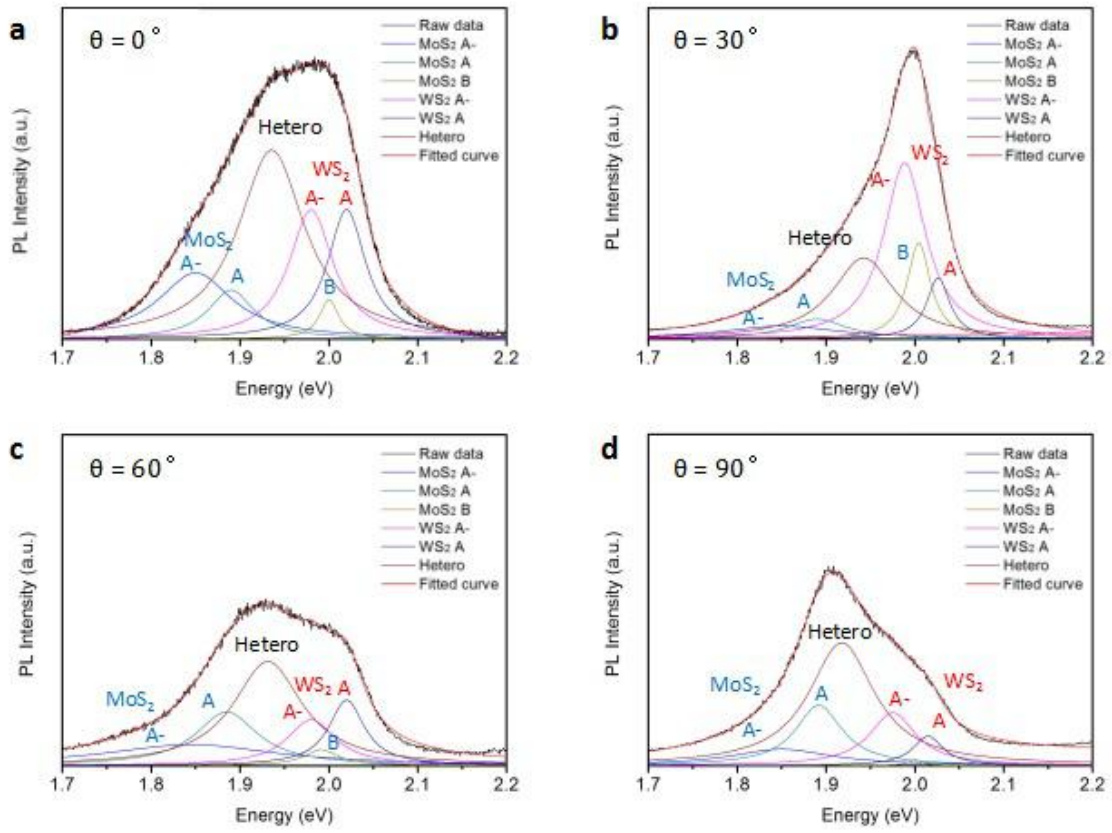

Figure 4-10. Fitted photoluminescence spectra of WS_2/MoS_2 heterostructures with different twisted angles θ = 0° (a), 30° (b), 60° (c), and 90° (d). The curves in different colors represent for different peaks, and the peaks are labeled. The fitting process is constrained by the facts that difference between MoS_2 A^- and A peak is 18-50 meV [12]; Difference between WS_2 A- and A peak is 40-45 meV [13]; Difference between exciton (A) and exciton (B) peak is 0.12 - 0.15 eV [10, 12].

According to the fitted result, the peak positions are around 1.85 eV, 1.88 eV, 1.93 eV,

1.98 eV, 2.01 eV, 2.02 eV, and labeled by MoS_2 A-, MoS_2 A, Hetero, WS_2 A-, MoS_2 B, WS_2 A, respectively. The PL spectra can be well reproduced by the sum of these peaks. The analysis suggests that the PL spectra show distinct features for various twisted heterostructures. For example, the intensities and positions of the peaks of the WS_2 emissions, the MoS_2 emissions and the Hetero peaks are different in these heterostructures. Therefore next step we focus on the information given by the fitted curves.

In order to investigate the change of the inter-layer charge transfer at different twisted angles, we looked at the weight of the exciton peaks and the trion peaks of MoS_2 and WS_2. Since the peaks in WS_2 have good intensities and smaller peak width compared with MoS_2, the WS_2 exciton and trion peaks are better choices for analyzing the charge transfer. The peak positions and intensities information of the WS_2 emissions in the heterostructures can be obtained from the fitted curves, and the emission intensities are calculated by the integral areas. The data are listed in Table 4-1.

Table 4-1. Normalized intensities and positions of WS_2 emission peaks in WS_2/MoS_2 heterostructures with different twisted angles.

	θ = 0°	θ = 30°	θ = 60°	θ = 90°
$I_{A^-}(WS_2)$	22	96	9	19
A^- energy (WS_2)	1.98 eV	1.99 eV	1.98 eV	1.98 eV
$I_A(WS_2)$	19	18	9	7
A energy (WS_2)	2.02 eV	2.03 eV	2.02 eV	2.02 eV
$I_{A^-}(WS_2)/I_A(WS_2)$	1.2	5.3	1.0	2.7

The ratios between the $I_{A^-}(WS_2)$ and the $I_A(WS_2)$ are calculated. In twisted samples (30° and 90°), the ratios are 5: 1 and 3: 1, respectively, while in the other two samples the ratios are

around 1: 1. The huge difference indicates that the densities of electrons are very different in the WS_2 layer of twisted (30° and 90°) and ordered (0° and 60°) samples. Twisted lattices have a higher weight of the A^- trions in emissions from the WS_2 layer. A higher weight of the trion peak means fewer holes injected into the WS_2 VBM and fewer electrons injected into the MoS_2 layer, in other words, less charge transfer between the layers. Less charge transfer in twisted WS_2/MoS_2 heterostructures indicates that the inter-layer coupling is reduced in these samples. In the WS_2/MoS_2 heterostructure, because the W atoms and the Mo atoms are screened in the layers of S atoms, the inter-layer forces are dominated by S-S interactions. The disordered alignment results in S-S repulsive forces which leads to weak inter-layer bondings. For the two cases of well aligned heterostructures: 0° and 60° twisted samples, better interlayer coupling is formed.

Besides the change of the inter-layer coupling, the twisted lattice and the changed atom coordination environment can lead to more changed properties in the bilayer heterostructures. For example, the A-A stacking (θ =0°) and A-B (θ = 60°) stacking bilayers have very different alignment of atoms [10] and thus the electronic band structures are distinct. In our WS_2/MoS_2 heterostructures, the position of the Hetero peak represents the energy gap between the MoS_2 CBM and the WS_2 VBM and gives information of the electronic band structures of the heterostructures. The information of all Hetero peaks are shown in Table 4-2. The Hetero peaks have similar widths, but have different peak energies. It is found that the peak energy changes at different twisted angles: at 0° and 30°, the energy gap is higher (~1.94 eV) while at 60° and 90° it is lower (~1.92 eV). This demonstrates that the electronic band structures of A-A and A-B stacked heterostructures are different, and accordingly, that the 30° twisted structures are different from the 90° twisted ones. Although both the A-A stacking and the A-B stacking possess organized structures, the A-B stacking has a more compact alignment because all the S atoms of the first layer superimpose the M atoms of the second layer, and vice versa. Therefore the A-B

stacking heterostructures have tighter bonding than the A-A stacking, and the changes of Hetero peak energy are probably due to the changes of atom coordination under different stacking order.

Table 4-2. Normalized intensities, widths and positions of the Hetero peaks in WS_2/MoS_2 heterostructures with different orientations.

	θ = 0°	θ = 30°	θ = 60°	θ = 90°
I (Hetero)	49	66	28	63
Width (Hetero)	0.09 eV	0.09 eV	0.09 eV	0.09 eV
Energy (Hetero)	1.94 eV	1.94 eV	1.93 eV	1.92 eV

4.6 Conclusion

Twisted WS_2/MoS_2 heterostructures were synthesized via artificially stacking method. The Raman and Photoluminescence spectra of the twisted WS_2/MoS_2 heterostructures were studied. For Raman, both the LBM and the SM modes were found in the low-frequency region. However, no significant changes were observed in twisted samples. In the PL spectra, the intensities of the WS_2 and MoS_2 emissions were quenched due to the charge transfer process, and the emissions from the MoS_2 CBM to the WS_2 VBM generate 'Hetero' peaks between 1.92 - 1.94 eV. From the weight of the Hetero peaks as well as the ratio of WS_2 A^-/A intensities, we found reduced inter-layer coupling in twisted lattices. We also found a difference in the inter-layer coupling of different twisted samples due to different atom coordination in A-A and A-B stacking.

References

1. H. Terrones, F. López-Urías and M. Terrones, Novel hetero-layered materials with tunable direct band gaps by sandwiching different metal disulfides and diselenides, Sci. Rep., 2013, 3, 1549.

2. J. Kang, J. Li, et al. Electronic Structural Moiré Pattern Effects on MoS_2/$MoSe_2$ 2D Heterostructures, Nano Lett., 2013, 13, 5485–5490.

3. H. Fang, et al. Strong interlayer coupling in van der Waals heterostructures built from single-layer chalcogenides, Proc. Natl. Acad. Sci. U. S. A., 2014, 111, 6198–6202.

4. S. Tongay, et al. Tuning Interlayer Coupling in Large-Area Heterostructures with CVD Grown MoS_2 and WS_2 Monolayers, Nano Lett., 2014, 14, 3185–3190.

5. X. Duan et al. Two-dimensional transition metal dichalcogenides as atomically thin semiconductors: opportunities and challenges. Chem. Soc. Rev., 2015, 44, 8859-8876.

6. J. Kang et al. Electronic Structural Moiré Pattern Effects on MoS_2/$MoSe_2$ 2D Heterostructures. Nano Lett., 2013, 13, 5485–5490.

7. N. Peimyoo et al, Chemically Driven Tunable Light Emission of Charged and Neutral Excitons in Monolayer WS_2, ACS Nano, 2014, 8, 11320-11329.

8. S. Mouri, et al. Tunable Photoluminescence of Monolayer MoS_2 via Chemical Doping. Nano Lett. 2013, 13, 5944−5948.

9. J. Zhang et al. Observation of Strong Interlayer Coupling in MoS_2 /WS_2 Heterostructures. Adv. Mater. 2016, 28, 1950 – 1956.

10. S. Huang et al. Probing the Interlayer Coupling of Twisted Bilayer MoS_2 Using Photoluminescence Spectroscopy, Nano Lett. 2014, 14, 5500−5508.

11. K. M. McCreary et al. The Effect of Preparation Conditions on Raman and Photoluminescence of Monolayer WS_2, Scientific Reports, 2016, 6: 35154.

12. K. F. Mak, K. He, C. Lee, G. H. Lee, J. Hone, T. F. Heinz, J. Shan. Tightly bound trions in monolayer MoS_2. Nature Materials 2013, 12, 207–211.

13. Z. Ye, T. Cao, et al. Zhang, X. Probing Excitonic Dark States in Single-Layer Tungsten Disulphide. Nature 2014, 513, 214–218.

Chapter 5

Summary and Outlook

Transition metal dichalcogenide monolayers have attracted a lot of attention due to their novel properties such as the direct band gap [1] and the spin-orbit coupling [2], and show potential in the applications of electronics and optics. Creating artificial heterostructures via stacking different TMDC monolayers on top of one another would establish a whole family of new materials with unusual characteristics other than the intrinsic possibilities of TMDC materials. The stacked heterostructures are covalently bonded in-plane whereas adjacent layers are relatively weakly bonded by van der Waals forces[3]. Due to the band offsets of the conduction band and valence band at the interface, there will be charge carriers transferring between different materials.

In our work, the transfer method was optimized to synthesize the artificially stacked TMDC heterostructures. The bilayer heterostructures possess different twisted angles between two layers, and the misorientations between lattices will result in moiré pattern to the system, which looks like an ordered 'super' lattice. The moiré pattern structure changes when the lattices are twisted with different angles. Therefore, our work focuses on how the properties of TMDC heterostructures change at different twisted angles. Techniques such as Raman and Photoluminescence spectroscopy are used to investigate the vibrational and optical properties of the heterostructures.

5.1 Conclusions

The wet chemical method is able to transfer atomic thick layers as well as multilayered TMDCs. When compared with dry transfers, the wet transfer process is quite easy and quick and

can be applied to other layered materials. However, for different samples, the thickness of the supporting films should be coated, which can be adjusted by the spin speed during the coating process. If a micromanipulator was applied to locate the flakes under the microscope, the flakes could be deposited onto the desired place with ~1 micron displacement. Photoluminescence signals of the TMDC monolayers was blue shifted after the transfer process due to relaxation from strain introduced by the substrate. The PL intensities of TMDC layers were heavily dependent on the substrate. There were shifts between the exciton modes and the trion modes, or quenching in the PL, depending on the properties of the substrate that was transferred onto.

With the wet chemical transfer method and the micromanipulator, stacked bilayers of MoS_2 were fabricated. The MoS_2 triangles had random orientations, and thus the stacked bilayers had different twisted angles. These stacked bilayers were characterized by Raman and Photoluminescence spectroscopy. The result showed no significant shift for twisted bilayers compared to untwisted ones. However, the Raman intensities were related to the twisted angles.

For the twisted WS_2/MoS_2 heterostructures, the Raman and the Photoluminescence spectra were studied. For Raman, both the LBM and the SM modes were found in the low-frequency region, but no significant differences were observed in samples with various orientations. In PL spectra, 'Hetero' peaks between 1.92 - 1.94 eV appeared due to the emissions from the MoS_2 CBM to the WS_2 VBM generate, which confirmed the charge transfer process of the heterostructure. The weight of the Hetero peaks, as well as the ratio of WS_2 A^-/A intensities, could be calculated from the fitted spectra, indicating the amount of the transferred charge. We found reduced charge transfer and thus reduced inter-layer coupling in 30° and 90° twisted lattices. Besides, differences of A-A and A-B stackingsamples were found. The atoms coordinations were changed with different stacking orders, and then the interlayer forces were tuned, resulting in the change of charge transfer.

The twisted lattices change the atom coordination and the interlayer van der Waals

bonding. Therefore, the orientation of the lattices has impact on the properties of the heterostructures. It would be an interesting system for studying the effect of lattice distortion on the TMD material properties. If the relationship between them could be accurately calculated, it would provide a possible approach to tuning the electronic and the optoelectronic properties of those van der Waals solids.

5.2 Perspectives

The synthesis of twisted heterostructures were achieved by the method of transfer, and the characterizations have shown that the twisted lattices affected the properties of the heterostructures. Based on the results, there are a lot of prospects in the artificially stacked TMDC heterostructures, including improvement of the transfer methods and further studies of the twisted heterostructures.

5.2.1 Transfer techniques

Although the wet-chemical transfer method can fabricate the stacked heterostructures, a more automated method needs to be developed to realize large quantities synthesis as well as fine controls of the assembly procedure. Donna Deng *et al.* Published an electrical-field-assisted assembly method of TMDC monolayer sheets [4], and the procedure is shown in Figure 5-1. This method is using wet chemical method to release the triangles from substrates, and then the released film is dissolved in acetone to get a solution of TMDC triangles. Under the drive forces of electrical fields, the triangles will be deposited onto Ti/Au electrodes, and they prefer to locate in the gap regions of the electrodes [4].

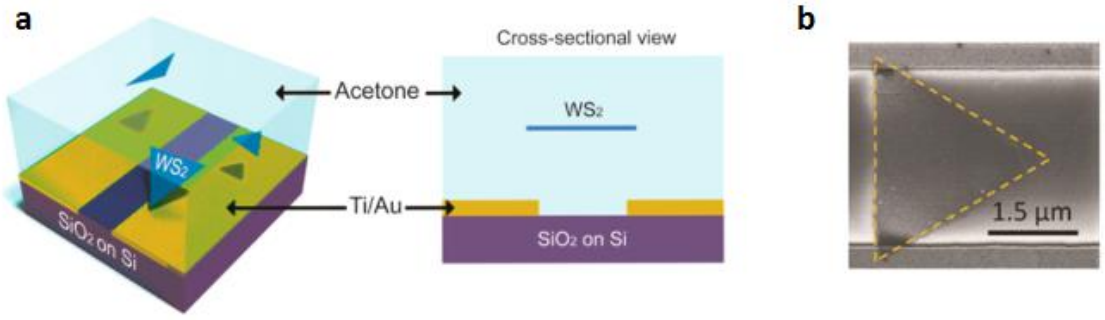

Figure 5-1 (a) Schematic of the electrical-field-assisted assembly system in an acetone media; (b) High-magnification optical images of the assembled WS_2 triangles, The WS_2 sheets are darker compared with the electrode regions [4].

This deterministic transfer method associated with electrical fields is excellent for stacking heterostructures in large quantities, because it has a more automated procedure and the target locations can be controlled by changing the electrodes. Two approaches of fabricating TMDC heterostructures can be tried with the help of electrical-field-assisted assembly:

(1) Two-step assembly, i.e. assemble a layer of MoS_2 triangles firstly, and then load WS_2 solutions to assemble a second layer of WS_2 triangles, and finally obtain heterostructures of WS_2/MoS_2;

(2) One-step assembly using metallic strips of MX_2 instead of the Ti/Au electrode, i.e. Use few-layer 2H-NbS_2 as the electrode, and then assemble WS_2 triangles. In this way WS_2/NbS_2 heterostructures can be fabricated. However, considering the electrolysis of NbS_2 [5], the voltage applied to the electrodes is limited. Therefore, optimization of the process is needed in order to assemble the TMDC triangles without damage to electrodes.

5.2.2 Localized properties of the artificially stacked heterostructures

We have studied the impacts of the twisted angle on the macroscopic view of heterostructures: the resolution of both Raman and Photoluminescence spectroscopy are in

micrometer scale, which is almost 10^2 times larger than the size of the moiré pattern unit cell. As is mentioned in the Chapeter 4, the TMDC twisted heterostructures may have strongly localized density of states in the moiré pattern [6]. Therefore, it will be interesting to investigate the performance of twisted heterostructures within one unit cell of the moiré pattern. Nano-scale characterization techniques could be used for this study.

Scanning Tunneling Microscopy (STM) can be used to look at the local density of states of the sample, and also gives information of the band alignment of heterostructures [7]. After probing the twisted heterostructures by STM, we can know the distribution of states, localized electronic transport ability in different twisted heterostructures. This will help further understanding of the influence of the moiré pattern in TMDC heterostructures.

In conclusion, we have demonstrated the probability of electronic band tuning by changing the twisted angle of heterostructures. In the future, we expect that the transfer techniques could be improved to realize commercialized productions, and we expect high-resolution characterization techniques could deeply investigate the impacts of moiré patterns on twisted heterostructures. Finally, we expect that the method of tuning properties could open a new direction in the novel device design.

References

1. K. F. Mak, C. Lee, J. Hone, J. Shan, T. F. Heinz, Atomically thin MoS_2: a new direct-gap semiconductor. Phys. Rev. Lett. 2010, 105, 136805.

2. K. F. Mak, K. He, J. Shan, T. F.Heinz, , Control of valley polarization in monolayer MoS_2 by optical helicity, Nature Nanotech. 2012, 7, 494–498.

3. A. K. Geim, et al. Van der Waals heterostructures. Nature 2013, 499, 419-425.

4. D. Deng, et al. Electric-Field-Assisted Directed Assembly of Transition Metal Dichalcogenide Monolayer Sheets. ACS Nano, 2016, 10 (5), 5006-5014.

5. H. Pan, Metal Dichalcogenides Monolayers: Novel Catalysts for Electrochemical Hydrogen Production. Scientific Reports 2014, 4: 5348.

6. J. Kang, J. Li, et al. Electronic Structural Moiré Pattern Effects on MoS_2/$MoSe_2$ 2D Heterostructures, Nano Lett., 2013, 13, 5485–5490.

7. Y.C. Lin, et al. Atomically Thin Resonant Tunnel Diodes built from Synthetic van der Waals Heterostructures. Nature Communications, 2015, 6, 7311.

Appendix A

Procedures

1. Preparation

Monolayer triangular MoS_2 crystals were grown on 300 nm SiO_2/Si wafers via Chemical Vapor Deposition. 1 cm*1 cm wafers were placed into a ceramic boat with 10 mg of MoS_2(≥ 99.5%, Sigma-Aldrich) on them. A ceramic boat with 300 mg of sulphur (≥99%, Sigma-Aldrich) was placed upstream. The boats were loaded into a 1-inch quartz tube. The growth was conducted at atmospheric pressure and 700 ℃ under ultrahigh-purity argon flow (around 80 s.c.c.m). The triangular crystals form after 30 minutes of growth. WS_2 monolayers were also grown by CVD with similar conditions. We used 10 mg WO_3(≥99.5%, Sigma-Aldrich) powders instead of MoS_2, and the growth temperature was 800 ℃.

After the CVD growth, the as grown samples were sonicated in acetone for 10 seconds to remove the powder residues. After sonication, the wafers were dried under ultra-high-purity N_2 flow slowly at room temperature.

2. Transfer

To fabricate a heterostructure via artificially stacking, we transferred one layer of TMDC material onto another. The transfer procedure is shown in Figure A-1. The layer for transferring was spin-coated with poly(methyl methacrylate) (PMMA) (495 A6) at 3,000 r.p.m. for 60 s and cured at room temperature for 8 hrs. The PMMA and TMDC film was released from the substrate (SiO_2/Si) by NaOH etching (1 mol/L) at 80 ℃ for a few minutes. The film was transferred to

deionized water to rinse the NaOH residue off the sample, and the rinsing step was repeated 6 times. It was then transferred onto another TMDC layer and placed on a 150℃ hot plate to dry away water. After that, acetone was used to dissolve the PMMA.

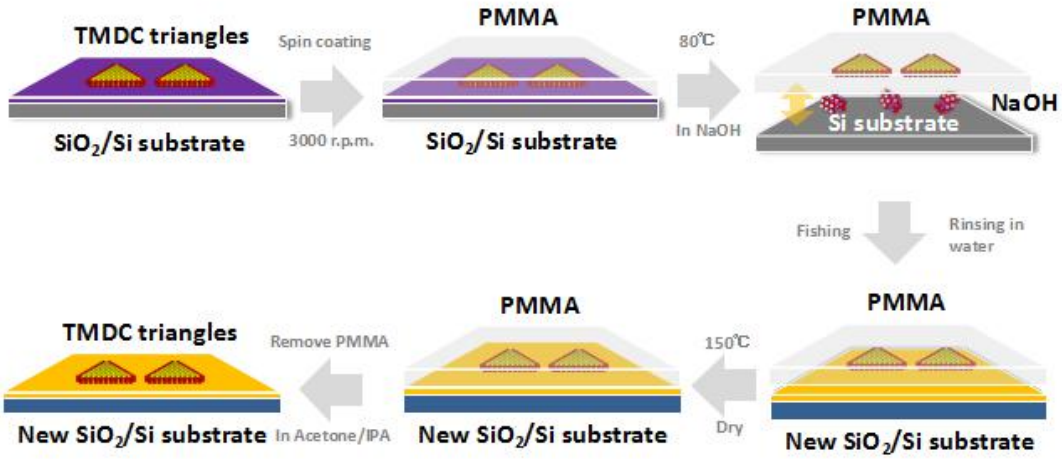

Figure A-1. Schematic illustration of the procedure of transferring 2D TMDC triangles, using 1M NaOH as the etchant.

Finally, the stacked bilayer heterostructures were annealed at 300℃ under forming gas with low pressure (10 torrs). The annealing process aimed to improve the contact between the layers so that the heterostructure could be coupled firmly.

3. Characterizations

Optical and fluorescent images were taken using Carl Zeiss Axio Imager Microscope.

Photoluminescence and ultra-low frequency Raman under 532 nm excitation were conducted with the Horiba LabRam HR Evolution Vis-NIR optimized & AIST-NT Scanning Probe, and the spectra were taken under a laser power of 47 μW for 1s, accumulated 10 times.

Photoluminescence under 488 nm excitation were conducted with the confocal Renishaw Raman, and the spectra were taken under a laser power of 10 μW for 10s, accumulated 5 times.

Appendix B

Data Statistics

I. Errors of the intensity ratio A_{1g}(2L)/A'_1(1L) for twisted bilayer MoS_2

The Raman data were collected for different twisted angles (θ). Due to a limited number of samples for each angle, we chose the 30° twisted heterostructure samples to calculate the standard errors of the intensity ratio, and there were 5 samples with a twisted angle of 30°.

Table B-1. The intensity ratio of A_{1g}(2L)/A'_1(1L) for stacked bilayer MoS_2 with different twisted angles (514 nm laser excitation).

θ(°)	30	30	30	30	30
I_{2L} / I_{1L}	1.89	1.77	1.95	1.82	1.65

The average value X= 1/5(1.89+1.77+1.95+1.82+1.65) = 1.82;

The standard error s= $[\Sigma(X_i\text{-}X)^2/(5\text{-}1)]^{1/2}$= 0.12.

Therefore, we use **0.12/1.82 = 7%** as the error bar for the intensity ratios of the 30° twisted bilayers, and we assume that the intensity ratios of other twisted angles also have a error of 7%.

Table B-2. The intensity ratio of A_{1g}(2L)/A'_1(1L) for stacked bilayer MoS_2 with different twisted angles (488 nm laser excitation).

θ(°)	30	30	30	30	30
I_{2L} / I_{1L}	1.59	1.43	1.41	1.60	1.45

The average value X= 1/5(1.59+1.43+1.41+1.60+1.45) = 1.50;

The standard error s= $[\Sigma(X_i\text{-}X)^2/(5\text{-}1)]^{1/2}$= 0.09;

Error: 0.09/1.50=6%.

In conclusion, the error of the twisted bilayer MoS_2 intensity ratios is 7% for 514 nm and 6% for 488 nm. Similarly, calculations of the annealed samples Raman data show that they have errors of 6% for 514 nm and 4% for 488 nm excitation, respectively.

II. Errors of the Raman peak positions for twisted WS_2/MoS_2 heterostructures

We also chose the 30° twisted heterostructure samples to calculate the standard errors, and there were 4 WS_2/MoS_2 samples with a twisted angle of 30°. For all spectra the Si peaks were calibrated to 520.5 cm^{-1}.

Table B-3. The Raman peak positions of WS_2/MoS_2 with different twisted angles (532 nm laser excitation).

θ(°)	30	30	30	30
WS_2 2LA (cm^{-1})	352.5	352.6	352.0	352.5
WS_2 E'(cm^{-1})	356.5	356.5	355.9	356.8
WS_2 A'$_1$(cm^{-1})	419.0	418.6	418.8	418.4
MoS_2 E'(cm^{-1})	381.2	381.7	381.7	381.9
MoS_2 A'$_1$(cm^{-1})	404.1	404.5	404.5	404.3
LBM(cm^{-1})	28.1	28.2	28.2	28.0
SM(cm^{-1})	22.3	22.2	22.4	22.1

So we got the Raman peak positions as follows:

WS_2 2LA = 352.4 ± 0.3 cm^{-1};

WS_2 E' = 356.4 ± 0.4 cm^{-1};

WS_2 A'$_1$ = 418.7 ± 0.3 cm^{-1};

MoS_2 E' = 381.6 ± 0.3 cm^{-1};

MoS_2 A'$_1$ = 404.4 ± 0.2 cm^{-1};

LBM = 28.1 ± 0.1 cm^{-1};

SM = 22.3 ± 0.1 cm^{-1}.

In conclusion, the errors of the 1st and 2nd order Raman peak positions are around 0.3 cm^{-1}, while the errors of the ultra-low frequency mode peak positions are around 0.1 cm^{-1}.

Curriculum Vitae

Education Background

Tsinghua University **2008.08 - 2012.07**

B.A. of Materials Science and Engineering

Research interests： Carbon materials(porous carbon and reduced graphene oxide)and their applications in supercapacitors and Li-ion battery anode materials.

Pennsylvania State University **2012.08 - 2017.05**

Ph.D. of Materials Science and Engineering

Research Interests： Assembly and fabrication of heterostructures of transition metal dichalcogenides and other semiconducting 2D materials, and their application in optoelectronic devices.

Publications

(1) Orientation-Dependent Photoluminescence Properties in Twisted WS_2/MoS_2 Heterostructures. Chanjing Zhou et al. To be published.

(2) Artificially Stacked Bilayer MoS_2 and the Orientation-Dependent Raman. Chanjing Zhou et al. To be published.

(3) Facile Synthesis of MoS_2 and $Mo_xW_{1-x}S_2$ Triangular Monolayers. Zhong Lin, Michael T. Thee, Ana L. Elias, Simin Feng, Chanjing Zhou et al. APL Materials, 2, 2014.

(4) Manganese Doping of Monolayer MoS_2: The Substrate Is Critical, Kehao Zhang, Simin Feng,..., Chanjing Zhou et al. Nano Lett., 15(10), 6586–6591, 2015.

(5) MoS_2 Monolayers on Nanocavities: Enhancement in Light-Matter Interaction. Corey Janisch, Haomin Song; Chanjing Zhou,et al. 2D materials, 2016, 3(2).

(6) Electric-Field-Assisted Directed Assembly of Transition Metal Dichalcogenide Monolayer Sheets. Donna Deng, Zhong Lin, Ana L. Elias, Nestor Perea-Lopez, Jie Li, Chanjing Zhou, et al. ACS Nano, 2016, 10 (5), 5006-5014.

(7) Optical identification of sulfur vacancies: Bound excitons at the edges of monolayer tungsten disulfide, Victor Carozo et al, Science Advances, 2017(received).